



# 1 Dealing with Spatial Heterogeneity in Pointwise to Gridded 2 Data Comparisons

3  
4 Amir H. Souri<sup>1\*</sup>, Kelly Chance<sup>1</sup>, Kang Sun<sup>2,3</sup>, Xiong Liu<sup>1</sup>, and Matthew S. Johnson<sup>4</sup>

5  
6 <sup>1</sup>Atomic and Molecular Physics (AMP) Division, Harvard–Smithsonian Center for Astrophysics,  
7 Cambridge, MA, USA

8 <sup>2</sup>Department of Civil, Structural and Environmental Engineering, University at Buffalo, Buffalo, NY, USA

9 <sup>3</sup>Research and Education in Energy, Environment and Water Institute, University at Buffalo, Buffalo, NY,  
10 USA

11 <sup>4</sup>Earth Science Division, NASA Ames Research Center, Moffett Field, CA, USA

12  
13 \*Corresponding author: [ahsouri@cfa.harvard.edu](mailto:ahsouri@cfa.harvard.edu)

## 14 Abstract

15 Atmospheric modelers and the trace gas retrieval community typically presuppose that pointwise  
16 measurements, which roughly represent the element of space, should compare well with satellite  
17 (model) pixels (grids). This assumption implies that the field of interest must possess a high degree  
18 of spatial homogeneity within the pixels (grids), which may not hold true for species with short  
19 atmospheric lifetimes or in the proximity of plumes. Results of this assumption often lead to a  
20 perception of a nonphysical discrepancy between data, resulting from different spatial scales,  
21 potentially making the comparisons prone to overinterpretation. Semivariogram is a mathematical  
22 expression of spatial variability in discrete data. Modeling the semivariogram behavior permits  
23 carrying out spatial optimal linear prediction of a random process field using kriging. Kriging can  
24 extract the spatial information (variance) pertaining to a specific scale, which in turn translating  
25 pointwise data to a grid space with quantified uncertainty such that a grid-to-grid comparison can  
26 be made. Here, using both theoretical and real-world experiments, we demonstrate that this  
27 classical geostatistical approach can be well adapted to solving problems in evaluating model-  
28 predicted or satellite-derived atmospheric trace gases. This study demonstrates that satellite  
29 validation procedures must take kriging variance and satellite spatial response functions into  
30 account. We present the comparison of Ozone Monitoring Instrument (OMI) tropospheric NO<sub>2</sub>  
31 columns against 11 Pandora Spectrometer Instrument (PSI) systems during the DISCOVER-AQ  
32 campaign over Houston. The least-squares fit to the paired data shows a low slope  
33 ( $OMI=0.76\times PSI+1.18\times 10^{15}$  molecules cm<sup>-2</sup>,  $r^2=0.67$ ) which is indicative of varying biases in  
34 OMI. This perceived slope, induced by the problem of spatial scale, disappears in the comparison  
35 of the convolved kriged PSI and OMI ( $0.96\times PSI+0.66\times 10^{15}$  molecules cm<sup>-2</sup>,  $r^2=0.72$ ) illustrating  
36 that OMI possibly has a constant systematic bias over the area. To avoid gross errors in  
37 comparisons made between gridded data versus pointwise measurements, we argue that the  
38 concept of semivariogram (or spatial auto-correlation) should be taken into consideration,  
39 particularly if the field exhibits a strong degree of spatial heterogeneity at the scale of satellite  
40 and/or model footprints.

41



## 42 1. Introduction

43 Most of the literature on validation of satellite trace gas retrievals or atmospheric chemical  
44 transport models assume that geophysical quantities within a satellite pixel or a model grid are  
45 spatially homogeneous. Nevertheless, it has long been recognized that this assumption can often  
46 be violated; spatially coarse atmospheric models or satellites are often not able to represent  
47 features, nor physical processes, transpiring at fine spatial scales. Janjic et al. [2016] used the term  
48 of *representation error* to describe this complication. They posit that this problem is a result of  
49 two combined factors: unresolved spatiotemporal scales and physiochemical processes. To  
50 elaborate on this definition, let us assume that an atmospheric model can represent the exact  
51 physiochemical processes but is fed with a constant CO<sub>2</sub> emission rate. This model obviously  
52 cannot resolve the spatial distribution of CO<sub>2</sub> concentration because we use an unresolved emission  
53 input. As another example, if we know the exact rates of CO<sub>2</sub> emissions but use a model unable to  
54 resolve atmospheric dynamics, the spatial distribution of CO<sub>2</sub> concentrations will be unrealistic  
55 due to unresolved physical processes.

56 Numerous scientific studies have reported on this matter. The simulations of short lifetime  
57 atmospheric compounds such as nitrogen dioxide (NO<sub>2</sub>), isoprene, formaldehyde (HCHO), and  
58 the hydroxyl radical (OH) have been found to be strongly sensitive to the model spatial resolution  
59 [Vinken et al., 2011; Valin et al., 2011; Yu et al., 2016; Pan et al., 2017]. Likewise, the performance  
60 of weather forecast models in resolving non-hydrostatic components heavily relies on both model  
61 resolution and parametrizations used. For example, when Kendon et al. [2014], Souri et al.  
62 [2020a], and Wang et al. [2017] defined a higher spatial resolution grid in conjunction with more  
63 elaborate model physics, they were able to more realistically simulate extreme or local weather  
64 phenomena such as convection and sea-land breeze circulation.

65 The spatial representation issue is not only limited to models. Satellite trace gas retrievals  
66 optimize the concentration of trace gases and/or atmospheric states to best match the observed  
67 radiance using an optimizer along with an atmospheric radiative transfer model. This procedure  
68 requires various inputs such as surface albedo, cloud and aerosol optical properties, and trace gas  
69 profiles, all of which come with different scales and representation errors. Moreover, the radiative  
70 transfer model by itself has different layers of complexity with regards to physics. A myriad of  
71 studies have reported that satellite-derived retrievals underrepresent spatial variability whenever  
72 the prognostic inputs used in the retrieval are spatially unresolved [e.g., Russell et al., 2011;  
73 Laughner et al., 2018; Souri et al., 2016; Goldberg et al., 2019; Zhao et al., 2020]. Additionally,  
74 the large footprint of some sensors relative to the scale of spatial variability of species inevitably  
75 leads to some degree of the representativity issues [e.g., Souri et al., 2020b, Tang et al., 2021; Judd  
76 et al., 2020].

77 The validation of satellites or atmospheric models is widely done against pointwise  
78 measurements. Mathematically, a point is an element of space. Hence, it is not meaningful to  
79 associate a point with a spatial scale. If one compares a grid to a point sample, they are assuming  
80 that the point is the representative of the grid. At this point, the fundamental question is: is such a  
81 comparison ever logical, in the sense that the average of the spatial distribution of the underlying  
82 compound is represented by a single value measured at a subgrid location? This question was  
83 answered in Matheron [1963]. He advocated the notion of the semivariogram, a mathematical  
84 description of the spatial variability, which finally led to the invention of kriging, the best unbiased  
85 linear estimator of a random field. A kriging model can estimate a geophysical quantity in a  
86 common grid. This is not exclusively special; a simple interpolation method such as the nearest  
87 neighbor has the same purpose. The power of kriging lies in the fact that it takes the data-driven



88 spatial variability information into account and informs an error associated with the interpolated  
89 map. This strength not only makes kriging a relatively superior model over simplified interpolation  
90 methods, but also reflects the level of confidence pertaining to spatial heterogeneity dictated by  
91 both data and the semivariogram model used through its variance [Chilès and Delfiner, 2009].

92 Different studies leveraged this classical geostatistical method to map the concentrations  
93 of different atmospheric compounds at very high spatial resolutions [Tadić et al., 2017; Li et al.,  
94 2019; Zhan et al., 2018]; To the best of our knowledge, Swall and Foley, [2009] is the only study  
95 that used kriging for a chemical transport model validation with respect to surface ozone. They  
96 suggested that kriging estimation should be executed in grids rather than discrete points. Kriging  
97 uses a semivariogram model in a continuous form. Optimizing the kriging grid size (i.e., domain  
98 discretization) at which the estimation is performed is an essence to fully obtaining the maximum  
99 spatial information from data. Another important caveat with Swall and Foley [2009] is that  
100 averaging discrete estimates (points) to build grids is not applicable for remote sensing data.  
101 Depending on the optics and the geometry, the spatial response function can transform from an  
102 ideal box (simple average) to a sophisticated shape such as a super Gaussian function (weighted  
103 average) [Sun et al., 2018]. Moreover, the footprint of satellites is not spatially constant. We will  
104 address these complications in this study using both theoretical and real-world experiments.

105 Our paper is organized with the following sections. Sections 2 is a thorough review of the  
106 concept of the semivariogram and kriging. We then provide different theoretical cases, their  
107 uncertainty, sensitivities with respect to difference tessellation, grid size, and the number of  
108 samples. Section 3 proposes a framework for satellite (model) validation using sparse point  
109 measurements and elaborates on the representation error using idealized experiments. Sections 4  
110 introduces several real-world experiments.

## 111 2. Semivariogram and Ordinary Kriging Estimator

### 112 2.1. Definition

113 The semivariogram is a mathematical representation of the degree of spatial variability (or  
114 similarity) in a function describing a regionalized geophysical quantity ( $f$ ), which is defined as  
115 [Matheron, 1963]:

$$116 \gamma(h) = \frac{1}{2V} \iiint_V [f(x + \mathbf{h}) - f(x)]^2 dV \quad (1)$$

117 where  $x$  is a location in the geometric fields of  $V$ ,  $f(x)$  is the value of a quantity at the location of  $x$ ,  
118 and  $\mathbf{h}$  is the vector of distance. If discrete samples are available rather than the continuous field,  
119 the general formula can be simplified to the experimental semivariogram defined as:

$$120 \gamma(h) = \frac{1}{2N(\mathbf{h})} \sum_{|x_i - x_j| - |\mathbf{h}| \leq \varepsilon} [Z(x_i) - Z(x_j)]^2 \quad (2)$$

121 where  $Z$  is discrete observations (or samples),  $N(\mathbf{h})$  is the number of paired observations separated  
122 by the vector of  $\mathbf{h}$ .  $|\cdot|$  operator indicates the length of a vector. The condition of  $|x_i - x_j| - |\mathbf{h}| \leq$   
123  $\varepsilon$  is to allow certain tolerance for differences in the length of the vector. For simplicity, we only  
124 focus on an isotropic case meaning we rule out the directional (or angular) dependency in  $\gamma(h)$ .

125 If a reasonable number of samples is present, one can describe  $\gamma(h)$  through a regression  
126 model (e.g., Gaussian or spherical shapes). The degree of freedom for this regression is:

$$127 dof = N - m \quad (3)$$

128 where  $m$  is the number of parameters defined in the model. For instance, to fit a Gaussian function  
129 to the semivariogram with three parameters ( $m=3$ ), three paired ( $N=3$ ) observations are required at  
130 minimum. It is not feasible to describe  $\gamma(h)$  with only one sample. In case of two samples, the



128 semivariogram might be explained by a line with no offsets (i.e.,  $\gamma(h) = a_o h$ ) or a constant  
 129 function ( $\gamma(h) = b_o$ ). Different regression models can be used to describe  $\gamma(h)$  depending on the  
 130 characteristic of the quantity of interest. In this study, we will use a stable Gaussian function:

$$\gamma(h) = a_o \left(1 - e^{-\left(\frac{h}{b_o}\right)^{c_o}}\right); a_o, b_o, c_o=1.5 \quad (4)$$

131 A non-linear least-squares algorithm based on Levenberg-Marquardt method will be used to  
 132 estimate the regression parameters.

133 The kriging estimator predicts a value of interest over a defined domain using a  
 134 semivariogram model derived from samples [Chilès and Delfiner, 2009]. The kriging model is  
 135 defined as [Matheron, 1963]:

$$Z(x) = Y(x) + m(x) \quad (5)$$

136 where  $Y(x)$  is a zero-mean random function, and  $m(x)$  is a systematic drift. If we assume  
 137  $m(x) = a_o$ , the model is called ordinary kriging. Similar to an interpolation problem, the  
 138 estimation point ( $\hat{Z}(x_o)$ ), is determined by linearly combining  $n$  number of samples,  $Z(x_j)$ , with  
 139 their weights ( $\lambda_j$ ):

$$\hat{Z}(x_o) = \sum_{j=1}^n \lambda_j Z(x_j) + \lambda_o \quad (6)$$

140 where  $\lambda_o$  is a constant weight. The mean squared error of this estimation can be written as

$$E(\hat{Z} - Z_o)^2 = \text{Var}(\hat{Z} - Z_o) + \left[ \lambda_o + \left( \sum_{j=1}^n \lambda_j - 1 \right) a_o \right]^2 \quad (7)$$

141 Where  $\hat{Z}$  is the estimation,  $Z_o$  is point observations, and  $a_o$  is the mean of  $Z$  which is unknown. In  
 142 order to estimate the weights, we are required to minimize Eq.7, but this cannot be done without  
 143 knowing the exact value of  $a_o$ . A solution is to assume  $\lambda_o = 0$  and impose the following condition:

$$\sum_{j=1}^n \lambda_j = 1 \quad (8)$$

144 This condition warrants  $E(\hat{Z} - Z_o)$  be zero and removes the need for the knowledge of  $a_o$ .  
 145 Therefore Eq.7 can be written as

$$E(\hat{Z} - Z_o)^2 = \text{Var}(\hat{Z} - Z_o) = \sum_{j_1=1}^n \sum_{j_2=1}^n \lambda_{j_1} \lambda_{j_2} \gamma_{j_1 j_2} - 2 \sum_{j_1=1}^n \lambda_{j_1} \gamma_{j_1 o} + \gamma_{oo} \quad (9)$$

146 Using the method of Lagrange multiplier and considering the constraint on the weights, Eq.9 can  
 147 be minimized by solving the following problem [Chilès and Delfiner, 2009]:

$$\begin{pmatrix} \lambda_1 \\ \vdots \\ \lambda_n \\ \mu \end{pmatrix} = \begin{pmatrix} \gamma(x_1 - x_1) \cdots \gamma(x_1 - x_n) & 1 \\ \vdots & \vdots \\ \gamma(x_n - x_1) \cdots \gamma(x_n - x_n) & 1 \\ 1 & \cdots & 1 & 0 \end{pmatrix}^{-1} \begin{pmatrix} \gamma(x_1 - x_o) \\ \vdots \\ \gamma(x_n - x_o) \\ 1 \end{pmatrix} \quad (10)$$

148 where  $\mu$  is the Lagrange parameter. The first term in the right hand side of this equation shows the  
 149 spatial variability described by the semivariogram model among samples, whereas the second term  
 150 indicates the modeled variability between samples and the estimation point. The unknowns (the  
 151 left hand side of the equation) have a unique solution if, and only if, the semivariogram model is  
 152 positive definite and the samples are unique [Chilès and Delfiner, 2009]. The estimation error can  
 153 be obtained by



$$\sigma^2 = E(\hat{Z} - Z_o)^2 = \sum_{j=1}^n \lambda_j \gamma_{j0} - \mu \quad (11)$$

154 This equation is an important component in the kriging estimator. Not only can we estimate  $Z(x_o)$   
155 given a selection of data points, but also an uncertainty associated with such estimation can be  
156 provided.

## 157 **2.2. Theoretical Cases**

### 158 *2.2.1. Sensitivity to spatial variability of the field*

159 The present section illustrates the application of ordinary kriging for several numerical  
160 cases. Five idealized cases are simulated in a grid of  $100 \times 100$  pixels, namely, a constant field (C1),  
161 a ramp starting from zero in the lower left to higher values in the upper right (C2), an intersection  
162 with concentrated values in four corridors (C3), a Gaussian plume placed in the center (C4), and  
163 multiple Gaussian plumes spread over the entire domain (C5). We randomly sample 200 data  
164 points from each field as is, and successively create the semivariograms in 100 binned distances.  
165 Except C1, which lacks a spatial variability thus  $\gamma(h) = b_o = 0$ , other semivariograms are fit with  
166 the stable Gaussian function. Using the semivariogram model, we optimize Eq.10 to estimate  $\hat{Z}(x)$   
167 for each pixel (i.e.,  $100 \times 100$ ) with the estimation errors based on Eq.11. Figure 1 depicts the truth  
168 field ( $Z(x)$ ), semivariograms made from the samples, estimated values ( $\hat{Z}(x)$ ), difference of  $Z(x)$   
169 and  $\hat{Z}(x)$ , and error associated with the estimation.

170 As for C1, the uniformity results in a constant semivariogram leading the estimation to be  
171 identical to the truth. This estimation signifies the unbiased characteristic of ordinary kriging. C1  
172 is never met in reality, however, it is possible to assume some degree of uniformity among data  
173 restrained to background values; a typical example of this can be seen in the spatial distribution of  
174 a number of trace gases in pristine environments such as  $\text{NO}_2$  [e.g., Wang et al., 2020] and HCHO  
175 [Wolfe et al., 2019]. Under this condition, any data point within the field (i.e., the satellite  
176 footprint) can be assumed to be representative of the spatial variability in truth.

177 Concerning C2, the semivariogram shows a linear shape meaning data points at larger  
178 distances exhibit larger differences. Generally geophysical samples are uncorrelated at large  
179 distances, thereby one expects the semivariogram to increase more slowly as the distance gets  
180 further. The steady increase in  $\gamma(h)$  is indicative of a systematic drift in the data invalidating the  
181 assumption of  $m(x) = a_o$ . In many applications, a simple polynomial can explain  $m(x)$  and  
182 subsequently be subtracted from the data points. An example of this problem is tackled by Onn  
183 and Zebker [2006]; it concerns the spatial variability of water vapor columns measured by GPS  
184 signals. Onn and Zebker [2006] observed a strong relationship between the water vapor columns  
185 and GPS altitudes resulting from the vertical distribution of water vapor in the atmosphere.  
186 Because of this complication, a physical drift model describing the vertical dependency was fit  
187 and removed from the measurements so that they could focus on the horizontal fluctuations. In  
188 terms of C2, one can effortlessly reproduce  $Z(x)$  by fitting a three-dimensional plane to barely  
189 three samples, indicating that the semivariogram is of little use.

190 C3 is an example of an extremely inhomogeneous field manifested in the stabilized  
191 semivariogram at a value of  $\gamma$  ( $\sim 500$ ), called the sill, indicating insignificant information (variance)  
192 from the samples beyond this distance ( $\sim 20$ ), called the range. Range is defined as the separation  
193 distance at which the total variance in data is extracted. The smaller the range is, the more  
194 heterogeneous the samples will be. While the estimated field roughly captures the shape of the  
195 intersections, it is spatially distorted at places with relatively sparse data points. The kriging model



196 error is essentially a measure of the density of information. It converges to zero in the sample's  
197 location and diverges to large values in gaps.

198 C4 is a close example of a point source emitter with faint winds and turbulence. The  
199 semivariogram exhibits a bell shape. As samples get further from the source, the variance diverges,  
200 stabilizes, and then sharply decreases. This is essentially because many data points with low  
201 values, apart from each other, have negligible differences. This tendency is recognized as the hole  
202 effect which is characterized for high values to be systemically surrounded by low values (and  
203 vice versa). It is possible to mask this effect by fitting a semivariogram model stabilizing at certain  
204 sill (like the one in Figure 1). Nonetheless, if the semivariogram shows periodic holes, the fitted  
205 model should be modified to a periodic cosine model [Pyrzcz and Deutsch, 2003].

206 The last case, C5, shows a less severe case of the hole effect previously observed in C4.  
207 This is due to the presence of more structured patterns in different parts of the domain. The range  
208 is roughly twice as large as the previous case (C4) denoting that there is more information  
209 (variance) among the samples at larger distances. A number of experiments using this particular  
210 case will be discussed in the following subsections.

#### 211 2.2.2. Sensitivity to the number of samples

212 It is often essential to optimize the number of samples used for kriging. The kriging  
213 estimator somewhat recognizes its own capability at capturing the spatial variability through  
214 Eq. 11. Thus, if the target phenomenon is spatially too complex and/or the samples are too limited,  
215 the estimator essentially informs that  $\hat{Z}(x_0)$  is unreliable through large variance. However, there  
216 is a caveat;  $Y(x)$  must be a Gaussian random model with a zero mean so that kriging can capture  
217 the statistical distribution of  $\hat{Z}$  given the data points. Except this case, the kriging variance can  
218 either be underestimated or overestimated depending on the level of skewness of the statistical  
219 distribution of  $Y(x)$  [Armstrong, 1994]. Figure 2 shows the kriging estimation for C5 using 5, 25,  
220 50, 100, and 500 random samples in the entire field. Immediately apparent is a better description  
221 of the semivariogram when larger number of samples are used, which in turn, results in a better  
222 estimation of  $Z(x)$ . The optimum number of samples to reproduce  $Z(x)$  depends on the  
223 requirement for the relative error ( $\sigma/Z(x)$ ) being met at a given location.

#### 224 2.2.3. Sensitivity to the tessellation of samples

225 A common application of kriging is to optimize the tessellation of data points for a fixed  
226 number of samples to achieve a desired precision. In real-world practices, the objective of such  
227 optimization is very purpose-specific, for example, one might prefer a spatial model representing  
228 a certain plume in the entire domain. Different ways for data selection exist [e.g., Rennen, 2008],  
229 but for simplicity, we focus on four categories: purely random, stratified random, a uniform grid,  
230 and an optimized tessellation. Figure 3 demonstrates the estimation of C5 using 25 samples chosen  
231 based on those four procedures.

232 Concerning the random selection, the lack of samples over two minor plumes cause the  
233 estimation to deviate largely from the truth. While a random selection may seem to be practical  
234 because it is independent of the underlying spatial variability, it can suffer from under sampling  
235 issues, thus being inefficient. As a remedy, it might be advantageous to group the domain into  
236 similar zones. We classify the domain into four zones using the k-mean algorithm (not shown) and  
237 randomly sample six to seven points from each one (total 25). We achieve a better agreement  
238 between the estimated field and the truth because we exploited some prior knowledge (here the  
239 contrast between low and high values).

240 As for the uniform grid, we notice that there are fewer data points in the semivariogram  
241 stemming from redundant distances which is indicative of correlated information. Nonetheless, if



242 the desired tessellation is neutral with regard to location meaning that all parts of the domain is  
243 equal of scientific interest, the uniform grid is the most optimal design for the prediction of  $Z(x)$   
244 under an ideally isotropic case. A mathematical proof for this claim can be found in Chilès and  
245 Delfiner [2009].

246 To execute the last experiment, we select 25 random samples for 1000 times and find the  
247 optimal estimation by finding the minimum sum of  $|\hat{Z}(x_0) - Z(x)|$ . It is worth mentioning that  
248 the optimized tessellation is essentially a local minimum based on 1000 realizations. The  
249 optimized location of samples seems to more clustered over areas with large spatial gradients. Not  
250 too surprisingly, we observe the smallest discrepancy between the estimation and the truth.

251 A lingering concern over the application of these numerical experiments is that the truth is  
252 assumed to be known. The truth is never known, by this means we may never exactly know how  
253 well or poorly the kriging estimator is performing. However, it is highly unlikely for some prior  
254 understandings or expectations of the truth to be absent. If this is the case, which is rare, a uniform  
255 grid should be intuitively preferred to deliver the local estimations of average values in uniform  
256 blocks. In contrast, if the prior knowledge is articulated by previous site visits, model predictions,  
257 theoretical experiments, pseudo-observations, or other relevant data, the tessellation needs to be  
258 optimized.

259 It is important to recognize that the uncertainties associated with the prior knowledge  
260 directly affects the level of confidence in the final answer. Accordingly, the prior knowledge error  
261 should ultimately be propagated to the kriging variance. The determination of the prior error is  
262 often done pragmatically. For example, if the goal is to design the location of thermometer sites to  
263 capture surface temperature during heat waves using a yearly averaged map of surface  
264 temperature, it would be wise to specify a large error with this specific prior information to play  
265 down the proposed design. This is primarily because the averaged map underrepresents such an  
266 atypical case. A possible extension of this example would be to use a weather forecast model with  
267 quantified errors capable of capturing retrospective heat waves. Although a reasonable forecast in  
268 the past does not necessarily guarantee a reasonable one in the future, it is rational to assume for  
269 the uncertainty with a new tessellation design using the weather model forecast to be lower than  
270 that of using the averaged map.

271 A general roadmap for the data tessellation design is shown in Figure 4. As proven in Chilès  
272 and Delfiner [2009], if the field is purely isotropic, the uniform grid is the most intuitive sensible  
273 choice when the prior information on the spatial variability is lacking. When the prior knowledge  
274 with quantified errors is available, an optimum tessellation can be achieved by running a large  
275 number of kriging models with suitable  $\gamma(h)$  and picking the one yielding the minimum distance  
276 between the prior knowledge and the estimation. The choice of the cost function (here L1 norm)  
277 is purpose-specific. For example, if the reconstruction of a major plume was the goal, using a  
278 weighted cost function, geared towards capturing the shape of plume, would be more appropriate.

#### 279 *2.2.4. Sensitivity to the grid size*

280 A kriging model can estimate a geophysical quantity at a desired location considering the  
281 data-driven spatial variability information. Since the kriging model is practically in a continuous  
282 form, the desired locations can be anywhere within the field of  $V$ . A question is whether or not it  
283 is necessary to map the data onto a very fine grid. There is a trade-off between the computational  
284 cost and the accuracy of the interpolated map. The range of the underlying semivariogram helps  
285 in finding the optimal solution. The greater the range (i.e., a more homogeneous field), the less  
286 important to map the data in a finer grid.



287 Figure 5a depicts an experiment comparing the estimates of C2 at different grid sizes with  
288 the truth. The departure of the estimate from the truth is rather negligible for several coarse grids  
289 (e.g.,  $10 \times 10$ ). The homogeneous field, manifested by the large range (Figure 1), allows for a  
290 reasonable estimation of  $Z(x)$  at coarse resolutions with inexpensive computational costs. Figure  
291 5b shows the same experiment but on C5 with the optimized tessellation. As opposed to the  
292 previous experiment, the estimate substantially diverges from the truth when increasing the grid  
293 size, suggesting that a finer resolution should be used for fields with smaller ranges (i.e.,  
294 heterogeneous fields).

295 The complexity of directly using the range for choosing the optimal grid cell size arises  
296 from the fact that the level of spatial homogeneity can vary within the domain. In fact, the range  
297 is derived from a semivariogram model representing a crude estimate of varying ranges occurring  
298 at various scales. It is intuitively clear that depending on the degree of heterogeneity, which is  
299 spatiotemporally variable, the grid size needs to be adaptively adjusted [Bryan, 1999]. For the sake  
300 of simplicity, but at a higher computational cost, we adopt a numerical solution which is to first  
301 simulate on a coarse grid, then on a finer one until the difference with respect to the previous grid  
302 size across all pixels reaches to an acceptable value ( $< 1\%$ ). We name this output ( $1 \times 1$ ) with the  
303 optimized tessellation for C5 as C5opt.

### 304 **3. Comparison of points to satellite pixels**

#### 305 ***3.1. Synching the scales between the gridded field and satellite pixels***

306 To minimize the complications of different spatial scales between two gridded data, we  
307 first need to upscale the finer resolution data to match the coarse ones. In case of numerical  
308 chemical transport or weather forecast models, the size of the grid is definitive. Likewise, a satellite  
309 footprint, mainly dictated by the sensor design, the geometry, and signal-to-noise requirements  
310 [Platt et al., 2021], is known. However, the grid size of the kriging estimation is a variable subject  
311 to optimization which has been discussed previously.

312 When we compare the grid size of the kriging estimate to that of a satellite (or a model),  
313 three situations arise: First, the kriging spatial resolution is coarser than the satellite, a condition  
314 occurring when either the field is homogeneous or the field is under sampled. In situations where  
315 the field is homogeneous ( $\gamma(h) \cong 0$ ), it is safe to directly compare the data points to the satellite  
316 measurements without having to use kriging. If the under sampling is the case (see Figure 2 with  
317 5 samples), it is sensible to first investigate if the field is homogeneous within the satellite footprint  
318 using different data (if any). If the homogeneity is met, we either can compare two datasets without  
319 kriging or to match the size of kriging grid cell with the satellite footprint and statistically involve  
320 the kriging variance in the comparison (discussed later); nonetheless, the kriging estimate beyond  
321 the location of samples must be used with extra caution because their variance very quickly  
322 departures from zero to extremely large numbers (see Figure 1). Thus, there is a compromise  
323 between increasing the number of paired samples between two datasets and enhancing the level of  
324 confidence in statistics. If independent observations suggest that there might be large heterogeneity  
325 within a satellite footprint, it is strongly advised against quantitatively comparing the points to the  
326 satellite observations. Second, the number of samples is fewer than three observations in the field  
327 so it is in principal impossible to build a semivariogram. Validating a satellite under this condition  
328 is prone to misinterpretation because the spatial heterogeneity cannot be modeled. Nonetheless, if  
329 one presumes a good degree of homogeneity within the sensor footprint (such as very high-  
330 resolution remote sensing airborne data), the direct comparison of point measurements might be  
331 possible. Third, the satellite footprint is coarser than the kriging estimate. Under this condition, we  
332 upscale the kriging map to match the spatial resolution of the satellite using





$$\hat{Z}_c = \hat{Z}_f * S = \int \hat{Z}_f(x)S(x-y)dy \quad (12)$$

333 where  $S$  is the spatial response function,  $\hat{Z}_c$  is the coarse kriging field,  $\langle * \rangle$  is the convolution  
 334 operator,  $y$  is shift, and  $\hat{Z}_f$  is the fine field. In discrete form we can rewrite Eq.12 in

$$\hat{Z}_c[i, j] = \sum_m \sum_n \hat{Z}_f[i-m, j-n] S[m, n] \quad (13)$$

335 where  $m$  and  $n$  are the dimension of the response function. The mathematical formulation of  
 336  $S[m, n]$  for a number of satellites can be represented by two-dimensional super Gaussian functions  
 337 as discussed in Sun et al. [2018]. Atmospheric models have a uniform response to the simulated  
 338 values within a grid, therefore  $S[m, n] = \frac{1}{m \times n} J_{m,n}$ , where  $J$  is the matrix of ones. In the same way,  
 339 the kriging variance should be convolved through

$$\sigma_c^2[i, j] = \sum_m \sum_n \sigma_f^2[i-m, j-n] S^2[m, n] \quad (14)$$

340 where  $\sigma_c^2$  and  $\sigma_f^2$  are the kriging variance in the coarse and the fine grids, respectively.

341 To demonstrate the upscaling procedure, we use C5opt (1×1) and upscale it at six grids  
 342 ( $m, m$ ) of 5×5, 10×10, 15×15, 20×20, 25×25, and 30×30 considering  $S = \frac{1}{m^2} J_{m,m}$ . Figure 6 shows  
 343 the resultant map overplotted with the samples along with the error estimation. Two tendencies  
 344 from this experiment can be identified: First, the discrepancy of the point data and  $\hat{Z}$  is becoming  
 345 more noticeable as the grid size grows; this directly speaks to the notion of the spatial  
 346 representativeness; large grid cells are less representative of sub-grid values. Second, the gradients  
 347 of the field along with the estimation error become smoother primarily due to convolving the field  
 348 with the spatial response function, which acts as a low pass filter.

349 We further directly compare  $\hat{Z}$  to the samples (i.e., observations) shown in Figure 7. We  
 350 see an excellent comparison between  $\hat{Z}$  at 1×1 resolution with the observations underscoring the  
 351 unbiasedness characteristic of the kriging estimator. Conversely, the upscaled field gradually  
 352 diverges from the observations. This divergence is *the problem of scale*.

### 3.2. Point to pixel vs pixel to pixel

353 To elaborate on the problem of scale, we design an idealized experiment theoretically  
 354 validating pseudo satellite observations against some pseudo point measurements. The pseudo  
 355 satellite observations are created by upscaling the C5 truth ( $Z$ ) to 30×30 grid footprint considering  
 356  $S = \frac{1}{m^2} J_{m,m}$ , meaning that the satellite is observing the truth but in a different scale (not shown).  
 357 The pseudo point measurements are the ones used for C5opt. Figure 8a shows the direct  
 358 comparison of the satellite pixel with the point observations. By ignoring the fundamental fact that  
 359 these two datasets are inherently different in nature, displaying the same geophysical quantity by  
 360 at different scales, we observe a perceived discrepancy ( $r^2=0.64$ ). The comparison suggests a  
 361 wrong conclusion that the satellite observations are biased-low. This discrepancy is unrelated to  
 362 any observational or physical errors, rendering any physical interpretation of the comparison  
 363 biased due to spatial-scale differences in the data sets. Figure 8b depicts the comparison of each  
 364 grid of the upscaled kriging estimate (30×30) with that of the satellite. This direct comparison  
 365 shows a strong degree of agreement ( $r^2=0.98$ ), shaking off the erroneous idea of directly comparing  
 366 point to gridded data when the field exhibits substantial spatial heterogeneity.  
 367



368 Yet, the comparison misses an important point: the kriging estimate is considered error-  
369 free. We attempt to incorporate the kriging variance through a Monte Carlo linear regression  
370 method. Here, the goal is to find an optimal linear fit ( $y = ax + b + \varepsilon$ ) such that  $\chi^2 =$   
371  $\sum \frac{[y-f(x_i, a, b)]^2}{\sigma_y^2 + a^2 \sigma_x^2}$  is minimized.  $\sigma_y^2$  and  $\sigma_x^2$  are the variances of  $y$  (here the satellite) and  $x$  (the kriging  
372 variance), respectively. We set the errors of  $y$  to zero, and randomly perturb the errors of  $x$  based  
373 on a normal distribution with zero mean and a standard deviation equal to that of kriging estimate  
374 15,000 times. The average of optimized  $a$  and  $b$  coefficients derived from each fit are then  
375 estimated and their deviation at 95% confidence interval assuming a Gaussian distribution is  
376 determined. Figure 8b,c show the linear fit with and without considering the kriging error estimate.  
377 The linear fit without involving the kriging error gives a strong impression that it is nearly perfect,  
378 following closely to the paired observations. This is essentially explainable by the primary goal of  
379  $\chi^2$  which is to minimize the L2 norm of residuals ( $y - f(x_i, a, b)$ ), portraying a very optimistic  
380 picture of the satellite validation. The linear fit considering the kriging errors is different. The  
381 uncertainties associated with  $a$  and  $b$  are larger since  $x$  is variable (shown in horizontal error bars).  
382 The optimal fit gravitates towards the points with smaller standard deviations as they possess a  
383 larger weight. The confidence in the linear fit at higher values is lower due to their errors being  
384 large. This fit is a more realistic portrayal of the satellite validation.

385 Figure 9 summarizes the general roadmap for satellite validations against point  
386 measurements. To fit the semivariogram with at least two parameters, we are required to have  
387 three samples at minimum. Therefore, it is implausible to derive the spatial information from the  
388 point data where sampling is extremely sparse (<3 samples within the field). The only case of  
389 directly comparing point and satellite pixels is when the field within satellite footprint or the field  
390 in general is rather homogeneous confirmed by independent data/models. Having more samples  
391 allows to acquire some information on the spatial heterogeneity. The information carried by the  
392 data is considered more and more robust with increasing the number of samples. Subsequently,  
393 the kriging map along with its variance derived from a reasonable semivariogram at an optimized  
394 grid resolution should be convolved with the satellite response function so that we can conduct an  
395 apples-to-apples comparison. A real-world example on the satellite validation will be shown later.

#### 396 **4. Real-world experiments**

##### 397 **4.1. Spatial distribution of $NO_2$**

398 We begin with focusing on tropospheric  $NO_2$  columns observed by TROPOMI sensor  
399 [Copernicus Sentinel data processed by ESA and Koninklijk Nederlands Meteorologisch Instituut  
400 (KNMI), 2019; Boersma et al., 2018] at  $\sim 13:30$  LST. We choose  $NO_2$  primarily due to its spatial  
401 heterogeneity [e.g., Sourì et al., 2018; Nowlan et al., 2016, 2018; Valin et al., 2011; Judd et al.,  
402 2020]. We oversample good quality pixels ( $qa\_flag > 0.75$ ) through a physical-based gridding  
403 approach [Sun et al., 2018] over Texas at  $3 \times 3$  km<sup>2</sup> resolution in four seasons in 2019. We extract  
404 samples by uniformly selecting the  $NO_2$  columns in the center of each  $30 \times 30$  km<sup>2</sup> block. The  
405 semivariogram along with its model are calculated, and then we kriging the samples. Figure 10 shows  
406 the  $NO_2$  columns map for four different seasons, the semivariogram, the kriging estimates, and the  
407 differences between the estimate and the field. High levels of  $NO_2$  are confined to cities indicating  
408 the sources being predominantly anthropogenic. Wintertime  $NO_2$  columns are larger than  
409 summertime mainly due to meteorological conditions and the OH cycle, the major sink of  $NO_2$ .  
410 All semivariograms exhibit the hole effect. This is because of high values of  $NO_2$  being  
411 systematically surrounded by low values. Regardless of the season, we fit the stable Gaussian to  
412 variances at distances smaller than  $2.5^\circ$  ( $\sim 275$  km<sup>2</sup>). The  $b_0$  parameter explaining the range (or the



length scale) is found to be 0.94, 0.88, 0.71, and 0.83 degree for DJF, MAM, JJA, and SON, respectively. These numbers strongly coincide with the length scale of NO<sub>2</sub>; wintertime NO<sub>2</sub> columns are spatially more uniform around the sources thus in relative sense, they are more homogeneous (spatially correlated) than those in warmer seasons. On the other hand, the shorter NO<sub>x</sub> lifetime in summer results in a steeper gradient of NO<sub>2</sub> concentrations. This tendency should not be generalized because transport and various NO<sub>x</sub> sources including biomass burning, soil emissions, and lightning and can have large spatiotemporal variability resulting in different length scales in different times of a year. The differences between the kriging estimate and the field show some spatial structures indicating that NO<sub>2</sub> is greatly heterogenous.

#### 4.2. Optimized tessellation over Houston

The preceding TROPOMI data enabled us to optimize a tessellation of ground-based point spectrometers over Houston. Our goal here is to propose an optimized network for winter 2021 given our knowledge on the spatial distribution of NO<sub>2</sub> columns in winter 2019 measured by TROPOMI. The assumption of using a retrospective NO<sub>2</sub> field for informing a hypothetical future campaign is not entirely unrealistic. If we have a consistent number of pixels from TROPOMI between two years, it is unlikely for the spatial variance of NO<sub>2</sub> to be substantially different for the same season. We follow the framework proposed in Sect. 2.2.3 involving randomly selecting samples from the field (for 50000 iteration), and calculating kriging estimates for a given number of spectrometers. We then chose the optimum tessellation based on the minimum sum of  $|\hat{Z}(x_0) - Z(x)|$ .

Figure 11 shows the optimized tessellation given 5, 10, 15, and 20 spectrometers over Houston. The Houston plume is better represented with more samples being used. All cases share the same feature; the optimized samples are clustered in the proximity or within the plume. This tendency is clearly intuitive. We are required to place the spectrometers in locations where a substantial gradient (variance) in the field is expected. The kriging estimate using 20 samples does not substantially differ in comparison to the one using 15 samples. A preferable strategy is to keep the number of spectrometers as low as possible while achieving a reasonable precision. Based on the presented results, the optimized tessellation using 15 samples is preferred among others.

#### 4.3. Validating OMI tropospheric NO<sub>2</sub> columns during DISCOVER-AQ 2013 campaign using Pandora

In order to understand ozone pollution [e.g., Mazzuca et al., 2016; Pan et al., 2017; Pan et al., 2015], characterize anthropogenic emissions [Souri et al., 2016, 2018], and validate satellite data [Choi et al., 2020], an intensive air quality campaign was made in September 2013 over Houston (DISCOVER-AQ). The campaign encompassed a large suite of Pandora spectrometer instrument (PSI) (11 stations) measuring total NO<sub>2</sub> columns with a high precision ( $2.7 \times 10^{14}$  molecules cm<sup>-2</sup>) and a moderate nominal accuracy ( $2.7 \times 10^{15}$  molecules cm<sup>-2</sup>) under the clear-sky condition [Herman et al., 2007]. We remove the observations with an error of >0.05 DU, contaminated by clouds, and averaged them over the month of September at 13:30 LST ( $\pm 30$  mins). We attempt to validate OMI tropospheric NO<sub>2</sub> columns version 3.0 [Bucsela et al., 2013] refined in Souri et al. [2016] with the 4-km model profiles. The OMI sensor resolution varies from 13×34 km<sup>2</sup> at nadir to ~40×160 km<sup>2</sup> at the edge of the scan line. Biased pixels were removed based on cloud fraction > 0.2, terrain reflectivity > 0.3, and main (xtrack) quality flags =0. Following Sun et al. [2018], we oversample high quality pixels in the month of September 2013 over Houston at 0.2° resolution. To remove the stratospheric contributions from PSI measurements, we subtract their columns from those of OMI stratospheric NO<sub>2</sub> over the area ( $2.8 \pm 0.16 \times 10^{15}$  molecules cm<sup>-2</sup>). Figure 12 shows the monthly-averaged tropospheric NO<sub>2</sub> columns measured by OMI overplotted



459 by 11 PSIs. The elevated NO<sub>2</sub> levels (up to  $\sim 6 \times 10^{15}$  molecules cm<sup>-2</sup>) are seen over the center of  
460 Houston.

461 We then follow the validation framework shown in Figure 9 in which the number of point  
462 measurements and the level of heterogeneity are the main factors in deciding if we should directly  
463 compare them to the satellite pixels. Figure 13 shows the monthly-averaged PSI measurements  
464 along with the semivariogram and resulting kriging estimate at an optimized resolution ( $\sim 2$  km<sup>2</sup> =  
465 13800 data over the entire region) and errors. The distribution of semivariogram suggests that there  
466 is a strong degree of spatial heterogeneity, necessitating the use of kriging. We fit a stable Gaussian

467 to the semivariogram resulting in  $2.23 \times (1 - e^{-\frac{h}{0.19}})^{1.5}$ . The spatial information (variance) levels  
468 off at 0.19° ( $\sim 21$  km) with a maximum variance equal to 2.23 molecules<sup>2</sup> cm<sup>-4</sup>. The measurements  
469 beyond this range (21 km) have a minimal weight due to this length scale. It is because of this  
470 reason that we see the kriging estimate converges to a fixed value at the grids being further than  
471 this range. The kriging errors of those grid cells are constantly large (40% relative error). The  
472 optimum grid size for kriging is found to be 2 km<sup>2</sup> (<1% difference across all grids). Subsequently,  
473 we use the super Gaussian spatial response function described in Sun et al. [2018] to convolve  
474 both the kriging estimate and error within. Figure 14 shows the differences between the kriging  
475 estimate and error before and after convolution. The response function (OMI pixel) tends to be on  
476 average coarser than 2 km<sup>2</sup> resulting in smoothing of both the kriging estimate and error.

477 We ultimately conduct two different sets of comparison: directly comparing PSI to OMI  
478 pixels, and comparing convolved kriged PSI to OMI. It is worth noting that PSI measurements are  
479 monthly-averaged; similarly OMI data are oversampled in a monthly basis. In terms of the PSI,  
480 we only account for grid cells whose kriging error is below  $1.2 \times 10^{15}$  molecules cm<sup>-2</sup> (1193  
481 samples, 8% of total kriging grids). As for the grid to grid comparison, the kriging variance is  
482 considered in the linear polynomial fitted to the data through the Monte Carlo of chi-square  
483 minimization with 5,000 iterations. The variability with the OMI stratospheric NO<sub>2</sub> columns ( $0.16$   
484  $\times 10^{15}$  molecules cm<sup>-2</sup>) is added to the PSI error for both analyses. The left and right panels of  
485 Figure 15 show the comparisons. As for the direct comparison of actual points (PSI) to pixels  
486 (OMI), the PSI measurements indicate a deviation of the slope ( $r^2=0.66$ ) from the unity line. This  
487 suggests that there is an unresolved magnitude-dependent systematic error. The grid-to-grid  
488 comparison not only offers a clearer picture of the distribution of data points, but also it hints at  
489 the offset being rather constant ( $0.66 \pm 0.18 \times 10^{15}$  molecules cm<sup>-2</sup>;  $r^2=0.72$ ). We also observe that  
490 the statistics between the satellite and the benchmark are moderately improved. This comparison  
491 in general provides an important implication: the varying offsets in a plume shape environment  
492 (high to low values) are not necessarily due to variable offsets in the satellite retrieval, as the  
493 kriging estimate suggests that those varying offsets in point-to-point comparison, manifested in  
494 slope = 0.76, are a result of varying spatial scales.

#### 495 **Summary**

496 There needs to be increased attention to the spatial representativity in the validation of  
497 satellite (model) against pointwise measurements. A point is the element of space, whereas satellite  
498 (model) pixels (grids) are (at best) the product of the integration of infinitesimal points and a  
499 normalized spatial response function. If the spatial response function is assumed to be an ideal  
500 box, the resulting grid will represent the average. Essentially, no justifiable theory exists to accept  
501 that the averaged value of a population should absolutely match with a sample, unless all samples  
502 are identical (i.e., a spatially homogeneous field). This glaring fact is often overlooked in the  
503 atmospheric science community. At a conceptual level, we are required to translate pointwise data  
504 to grid format (i.e., rasterization). This can be done by modeling the spatial autocorrelation (or



505 semivariogram) extracted from the spatial variance (information) among measured sample points.  
506 Assuming that the underlying field is a random function with an unknown mean, the best linear  
507 unbiased predictions of the field can be achieved by kriging using the modeled semivariograms.

508 In this study, we discussed methods for the kriging estimation of several idealized cases.  
509 Several key tendencies were observed through this experiment: first, the range corresponded to the  
510 degree of spatial heterogeneity; a larger range indicated the less presence of heterogeneity. Second,  
511 the kriging variance explaining the density of information quickly diverged from zero to large  
512 values when the field exhibited large spatial heterogeneity. This tendency mandates increasing the  
513 number of samples (observations) for those cases. Third, while the semivariogram models were  
514 constructed from discrete pair of samples, they are mathematically in a continuous form. It is  
515 because of this reason that we determined the optimal spatial resolution of the kriging estimate by  
516 incrementally making the grids finer and finer until a desired precision was met.

517 The present study applied kriging to achieve an optimum tessellation given a certain  
518 number of samples such that the difference between our prior knowledge of the field, articulated  
519 by previous observations, models or theory, and the estimation is minimal. Usually there is  
520 uncertainty about the prior knowledge that should be propagated to the final estimates. The  
521 optimum tessellation for a range of idealized and real-world data consistently voted for placing  
522 more samples in areas where the gradients in the measurements were significant such as those  
523 close to point emitters.

524 This study also revisited the spatial representativity issue; it limits the realistic  
525 determination of biases associated with satellites (models). In one experiment, we convolved the  
526 kriging estimate for a multi-plume field with a box filter but various sizes. The perfect agreement  
527 ( $r=1.0$ ) between the samples (point) and kriging output (pixel) seen at a high spatial resolution  
528 gradually vanished with coarsening of the grids ( $r=0.8$ ). We also directly compared samples (point)  
529 with pseudo satellite observations (showing the truth) with a coarse spatial resolution which led to  
530 a flawed conclusion about the satellite being biased-low. We modeled the semivariogram of those  
531 samples, estimated the field using kriging, and convolved with the pseudo-satellite spatial response  
532 function. The direct comparison of this output with that of the satellite showed a completely  
533 different story suggesting that the data were rather free of any bias. A serious caveat with using a  
534 spatial model (here kriging) is that it consists of errors: the estimations being further from samples  
535 are less certain. It is widely known that discounting the measurement/model errors in true straight-  
536 line relationship between data can introduce artifacts. To consider the kriging variance in the  
537 comparisons we employed a Monte Carlo method on chi-square optimization which ultimately  
538 allowed us to not only provide a set of solutions within the range of the uncertainty of the kriging  
539 model, but also to assign smaller weights on gross estimates.

540 We further validated monthly-averaged Ozone Monitoring Instrument (OMI) tropospheric  
541  $\text{NO}_2$  columns using 11 Pandora Spectrometer Instrument (PSI) observations over Houston during  
542 NASA's DISCOVER-AQ campaign. A pixel-to-point comparison between two dataset suggested  
543 varying biases in OMI manifested in a slope far from the identity line. By contrast, the kriging  
544 estimate from the PSI measurements, convolved with the OMI spatial response function, resulted  
545 in an inter-comparison slope close to the unity line. This suggested that there was only a constant  
546 systematic bias ( $0.66 \pm 0.18 \times 10^{15}$  molecules  $\text{cm}^{-2}$ ) associated with the OMI observations which  
547 does not vary with increasing tropospheric  $\text{NO}_2$  column magnitudes.

548 The central tenants of satellite and model validation are pointwise measurements. Our  
549 experiments paved the way for a clear roadmap explaining how to transform these pointwise



550 datasets to a comparable spatial scale relative to satellite observations. It is no longer necessary to  
551 ignore *the problem of scale*. The comparisons can be carefully conducted in the following steps:

- 552
- 553 i. Construct the experimental semivariogram if the number of point measurements  
554 allows (usually  $\geq 3$  within the field; the field can vary depending on the length  
555 scale of the compound).
  - 556 ii. Drop the quantitative assessment if the number of point measurements are  
557 insufficient to gain spatial variance and the prior knowledge suggests a high  
558 likelihood of spatial heterogeneity within the field.
  - 559 iii. Choose an appropriate function to model the semivariogram.
  - 560 iv. Estimate the field with kriging (or any other spatial estimator capable of digesting  
561 the semivariogram) and calculate the variance.
  - 562 v. Estimate the optimum grid resolution of the estimate.
  - 563 vi. Convolve the kriging estimate and its variance with the satellite (model) spatial  
564 response function (which is sensor specific).
  - 565 vii. Conduct the direct comparison of the convolved kriged output and the satellite  
566 (model) considering their errors through a Monte Carlo (or at minimum a weighted  
567 least-squared method).

568

569 Recent advances in satellite trace gas retrievals and atmospheric models have helped  
570 extend our understanding of atmospheric chemistry but an important task before us in improving  
571 our knowledge on atmospheric composition is to embrace the semivariogram (or spatial auto-  
572 correlation) notion when it comes to the point-pixel comparisons, so that we can have more robust  
573 quantitative applications of the data and models.

#### 574 **Acknowledgement**

575 Amir Souri and Matthew Johnson were funded for this work through NASA's Aura Science Team  
576 (grant number: 80NSSC21K1333). Kang Sun acknowledges support by NASA's Atmospheric  
577 Composition: Modeling and Analysis (ACMAP) program (grant number: 80NSSC19K09). We  
578 thank many scientists whose concerns motivated us to tackle the presented problem. In particular,  
579 we thank Chris Chan Miller, Ron Cohen, Jeffrey Geddes, Gonzalo González Abad, Christian  
580 Hogrefe, Lukas Valin, and Huiqun (Helen) Wang.

#### 581 **Author contributions**

582 AHS designed the research, executed the experiments, analyzed the data, made all figures, and  
583 wrote the paper. KS implemented the oversampling method, provided the spatial response  
584 functions, and oversampled TROPOMI data. KC, XL, and MSJ helped with the conceptualization  
585 of the study and the interpretation of the results. All authors contributed to discussions and edited  
586 the paper.  
587



## 588 **References**

- 589 Armstrong, M.: Is Research in Mining Geostats as Dead as a Dodo?, in: *Geostatistics for the*  
590 *Next Century: An International Forum in Honour of Michel David's Contribution to*  
591 *Geostatistics*, Montreal, 1993, edited by: Dimitrakopoulos, R., Springer Netherlands,  
592 Dordrecht, 303–312, [https://doi.org/10.1007/978-94-011-0824-9\\_34](https://doi.org/10.1007/978-94-011-0824-9_34), 1994.
- 593 Boersma, K. F., Eskes, H. J., Richter, A., De Smedt, I., Lorente, A., Beirle, S., van Geffen, J. H.  
594 G. M., Zara, M., Peters, E., Van Roozendaal, M., Wagner, T., Maasakkers, J. D., van der  
595 A, R. J., Nightingale, J., De Rudder, A., Irie, H., Pinardi, G., Lambert, J.-C., and  
596 Compernelle, S. C.: Improving algorithms and uncertainty estimates for satellite NO<sub>2</sub>  
597 retrievals: results from the quality assurance for the essential climate variables  
598 (QA4ECV) project, 11, 6651–6678, <https://doi.org/10.5194/amt-11-6651-2018>, 2018.
- 599 Botsch, M., Pauly, M., Wicke, M., and Gross, M.: Adaptive Space Deformations Based on Rigid  
600 Cells, 26, 339–347, <https://doi.org/10.1111/j.1467-8659.2007.01056.x>, 2007.
- 601 Bryan, G. L.: Fluids in the universe: adaptive mesh refinement in cosmology, 1, 46–53,  
602 <https://doi.org/10.1109/5992.753046>, 1999.
- 603 Bucsela, E. J., Krotkov, N. A., Celarier, E. A., Lamsal, L. N., Swartz, W. H., Bhartia, P. K.,  
604 Boersma, K. F., Veefkind, J. P., Gleason, J. F., and Pickering, K. E.: A new stratospheric  
605 and tropospheric NO<sub>2</sub> retrieval algorithm for nadir-viewing satellite instruments:  
606 applications to OMI, 6, 2607–2626, <https://doi.org/10.5194/amt-6-2607-2013>, 2013.
- 607 Chilès, J.-P. and Delfiner, P.: *Geostatistics: Modeling Spatial Uncertainty*, John Wiley & Sons,  
608 718 pp., 2009.
- 609 Choi, S., Lamsal, L. N., Follette-Cook, M., Joiner, J., Krotkov, N. A., Swartz, W. H., Pickering,  
610 K. E., Loughner, C. P., Appel, W., Pfister, G., Saide, P. E., Cohen, R. C., Weinheimer, A.  
611 J., and Herman, J. R.: Assessment of NO<sub>2</sub> observations during DISCOVER-AQ and  
612 KORUS-AQ field campaigns, 13, 2523–2546, <https://doi.org/10.5194/amt-13-2523-2020>,  
613 2020.
- 614 Goldberg, D. L., Saide, P. E., Lamsal, L. N., de Foy, B., Lu, Z., Woo, J.-H., Kim, Y., Kim, J.,  
615 Gao, M., Carmichael, G., and Streets, D. G.: A top-down assessment using OMI NO<sub>2</sub>  
616 suggests an underestimate in the NO<sub>x</sub> emissions inventory in Seoul, South Korea, during  
617 KORUS-AQ, 19, 1801–1818, <https://doi.org/10.5194/acp-19-1801-2019>, 2019.
- 618 Herman, J., Cede, A., Spinei, E., Mount, G., Tzortziou, M., and Abuhassan, N.: NO<sub>2</sub> column  
619 amounts from ground-based Pandora and MFDOAS spectrometers using the direct-sun  
620 DOAS technique: Intercomparisons and application to OMI validation, 114,  
621 <https://doi.org/10.1029/2009JD011848>, 2009.
- 622 Janjić, T., Bormann, N., Bocquet, M., Carton, J. A., Cohn, S. E., Dance, S. L., Losa, S. N.,  
623 Nichols, N. K., Potthast, R., Waller, J. A., and Weston, P.: On the representation error in  
624 data assimilation, 144, 1257–1278, <https://doi.org/10.1002/qj.3130>, 2018.
- 625 Judd, L. M., Al-Saadi, J. A., Szykman, J. J., Valin, L. C., Janz, S. J., Kowalewski, M. G., Eskes,  
626 H. J., Veefkind, J. P., Cede, A., Mueller, M., Gebetsberger, M., Swap, R., Pierce, R. B.,  
627 Nowlan, C. R., Abad, G. G., Nehrir, A., and Williams, D.: Evaluating Sentinel-5P  
628 TROPOMI tropospheric NO<sub>2</sub> column densities with airborne and Pandora spectrometers  
629 near New York City and Long Island Sound, 13, 6113–6140, <https://doi.org/10.5194/amt-13-6113-2020>, 2020.
- 631 Kendon, E. J., Roberts, N. M., Fowler, H. J., Roberts, M. J., Chan, S. C., and Senior, C. A.:  
632 Heavier summer downpours with climate change revealed by weather forecast resolution  
633 model, *Nature Clim Change*, 4, 570–576, <https://doi.org/10.1038/nclimate2258>, 2014.



- 634 Laughner, J. L., Zhu, Q., and Cohen, R. C.: The Berkeley High Resolution Tropospheric NO<sub>2</sub>  
635 product, 10, 2069–2095, <https://doi.org/10.5194/essd-10-2069-2018>, 2018.
- 636 Li, R., Cui, L., Meng, Y., Zhao, Y., and Fu, H.: Satellite-based prediction of daily SO<sub>2</sub> exposure  
637 across China using a high-quality random forest-spatiotemporal Kriging (RF-STK) model  
638 for health risk assessment, *Atmospheric Environment*, 208, 10–19,  
639 <https://doi.org/10.1016/j.atmosenv.2019.03.029>, 2019.
- 640 Matheron, G.: Principles of geostatistics, *Economic Geology*, 58, 1246–1266,  
641 <https://doi.org/10.2113/gsecongeo.58.8.1246>, 1963.
- 642 Mazzuca, G. M., Ren, X., Loughner, C. P., Estes, M., Crawford, J. H., Pickering, K. E.,  
643 Weinheimer, A. J., and Dickerson, R. R.: Ozone production and its sensitivity to NO<sub>x</sub>  
644 and VOCs: results from the DISCOVER-AQ field experiment, *Houston 2013*, 16, 14463–  
645 14474, <https://doi.org/10.5194/acp-16-14463-2016>, 2016.
- 646 Nowlan, C. R., Liu, X., Janz, S. J., Kowalewski, M. G., Chance, K., Follette-Cook, M. B., Fried,  
647 A., González Abad, G., Herman, J. R., Judd, L. M., Kwon, H.-A., Loughner, C. P.,  
648 Pickering, K. E., Richter, D., Spinei, E., Walega, J., Weibring, P., and Weinheimer, A. J.:  
649 Nitrogen dioxide and formaldehyde measurements from the GEOstationary Coastal and  
650 Air Pollution Events (GEO-CAPE) Airborne Simulator over Houston, Texas, 11, 5941–  
651 5964, <https://doi.org/10.5194/amt-11-5941-2018>, 2018.
- 652 Nowlan, C. R., Liu, X., Leitch, J. W., Chance, K., González Abad, G., Liu, C., Zoogman, P.,  
653 Cole, J., Delker, T., Good, W., Murcray, F., Ruppert, L., Soo, D., Follette-Cook, M. B.,  
654 Janz, S. J., Kowalewski, M. G., Loughner, C. P., Pickering, K. E., Herman, J. R., Beaver,  
655 M. R., Long, R. W., Szykman, J. J., Judd, L. M., Kelley, P., Luke, W. T., Ren, X., and  
656 Al-Saadi, J. A.: Nitrogen dioxide observations from the Geostationary Trace gas and  
657 Aerosol Sensor Optimization (GeoTASO) airborne instrument: Retrieval algorithm and  
658 measurements during DISCOVER-AQ Texas 2013, 9, 2647–2668,  
659 <https://doi.org/10.5194/amt-9-2647-2016>, 2016.
- 660 Onn, F. and Zebker, H. A.: Correction for interferometric synthetic aperture radar atmospheric  
661 phase artifacts using time series of zenith wet delay observations from a GPS network,  
662 111, <https://doi.org/10.1029/2005JB004012>, 2006.
- 663 Pan, S., Choi, Y., Roy, A., and Jeon, W.: Allocating emissions to 4 km and 1 km horizontal  
664 spatial resolutions and its impact on simulated NO<sub>x</sub> and O<sub>3</sub> in Houston, TX,  
665 *Atmospheric Environment*, 164, 398–415,  
666 <https://doi.org/10.1016/j.atmosenv.2017.06.026>, 2017.
- 667 Pan, S., Choi, Y., Roy, A., Li, X., Jeon, W., and Souri, A. H.: Modeling the uncertainty of  
668 several VOC and its impact on simulated VOC and ozone in Houston, Texas,  
669 *Atmospheric Environment*, 120, 404–416,  
670 <https://doi.org/10.1016/j.atmosenv.2015.09.029>, 2015.
- 671 Platt, U., Wagner, T., Kuhn, J., and Leisner, T.: The “Ideal Spectrograph” for  
672 Atmospheric Observations, 1–23, <https://doi.org/10.5194/amt-2020-521>, 2021.
- 673 Pyrcz MJ, Deutsch CV. The whole story on the hole effect. *Geostatistical Association of*  
674 *Australasia, Newsletter*. 2003 May;18:3-5.
- 675 Rennen, G.: Subset Selection from Large Datasets for Kriging Modeling, *Social Science*  
676 *Research Network*, Rochester, NY, <https://doi.org/10.2139/ssrn.1104595>, 2008.
- 677 Russell, A. R., Perring, A. E., Valin, L. C., Bucsela, E. J., Browne, E. C., Wooldridge, P. J., and  
678 Cohen, R. C.: A high spatial resolution retrieval of NO<sub>2</sub> column densities from OMI:  
679 method and evaluation, 11, 8543–8554, <https://doi.org/10.5194/acp-11-8543-2011>, 2011.





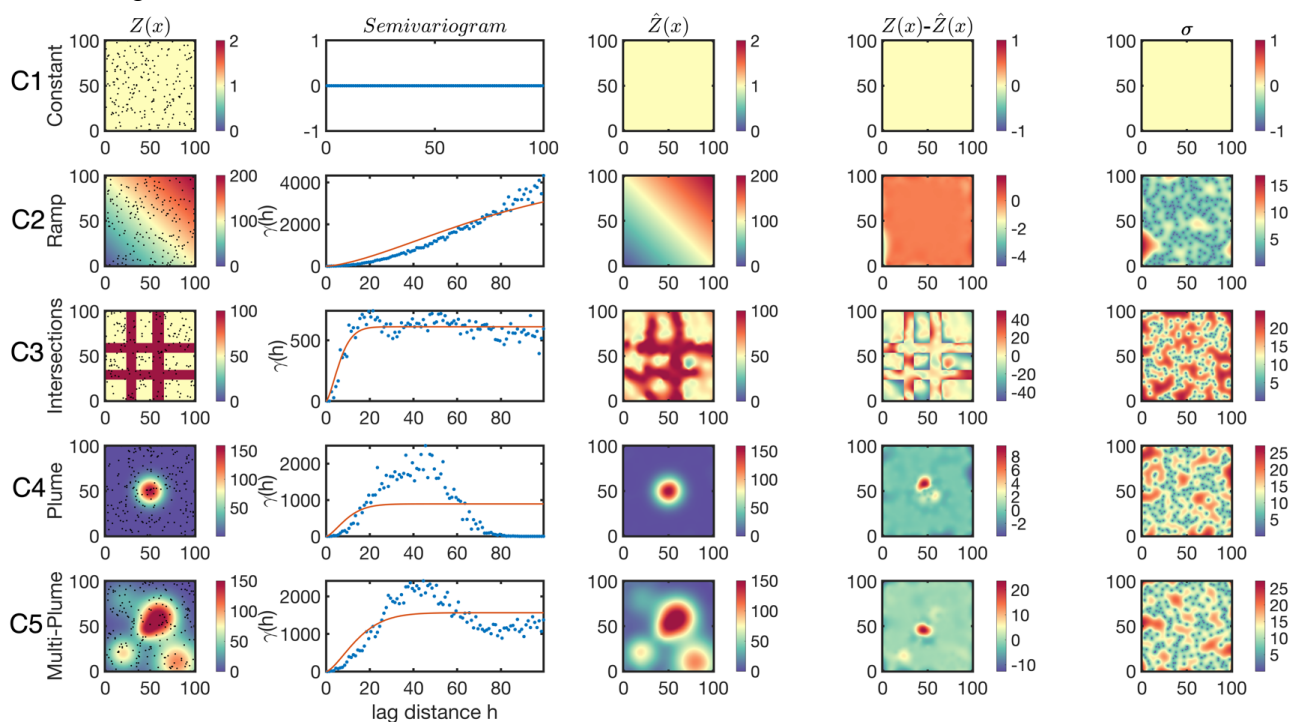
- 680 Souri, A. H., Choi, Y., Jeon, W., Li, X., Pan, S., Diao, L., and Westenbarger, D. A.: Constraining  
681 NO<sub>x</sub> emissions using satellite NO<sub>2</sub> measurements during 2013 DISCOVER-AQ Texas  
682 campaign, *Atmospheric Environment*, 131, 371–381,  
683 <https://doi.org/10.1016/j.atmosenv.2016.02.020>, 2016.
- 684 Souri, A. H., Choi, Y., Kodros, J. K., Jung, J., Shpund, J., Pierce, J. R., Lynn, B. H., Khain, A.,  
685 and Chance, K.: Response of Hurricane Harvey’s rainfall to anthropogenic aerosols: A  
686 sensitivity study based on spectral bin microphysics with simulated aerosols,  
687 *Atmospheric Research*, 242, 104965, <https://doi.org/10.1016/j.atmosres.2020.104965>,  
688 2020a.
- 689 Souri, A. H., Choi, Y., Pan, S., Curci, G., Nowlan, C. R., Janz, S. J., Kowalewski, M. G., Liu, J.,  
690 Herman, J. R., and Weinheimer, A. J.: First Top-Down Estimates of Anthropogenic NO<sub>x</sub>  
691 Emissions Using High-Resolution Airborne Remote Sensing Observations, 123, 3269–  
692 3284, <https://doi.org/10.1002/2017JD028009>, 2018.
- 693 Souri, A. H., Nowlan, C. R., Wolfe, G. M., Lamsal, L. N., Chan Miller, C. E., Abad, G. G., Janz,  
694 S. J., Fried, A., Blake, D. R., Weinheimer, A. J., Diskin, G. S., Liu, X., and Chance, K.:  
695 Revisiting the effectiveness of HCHO/NO<sub>2</sub> ratios for inferring ozone sensitivity to its  
696 precursors using high resolution airborne remote sensing observations in a high ozone  
697 episode during the KORUS-AQ campaign, *Atmospheric Environment*, 224, 117341,  
698 <https://doi.org/10.1016/j.atmosenv.2020.117341>, 2020b.
- 699 Sun, K., Zhu, L., Cady-Pereira, K., Chan Miller, C., Chance, K., Clarisse, L., Coheur, P.-F.,  
700 González Abad, G., Huang, G., Liu, X., Van Damme, M., Yang, K., and Zondlo, M.: A  
701 physics-based approach to oversample multi-satellite, multispecies observations to a  
702 common grid, 11, 6679–6701, <https://doi.org/10.5194/amt-11-6679-2018>, 2018.
- 703 Swall, J. L. and Foley, K. M.: The impact of spatial correlation and incommensurability on  
704 model evaluation, *Atmospheric Environment*, 43, 1204–1217,  
705 <https://doi.org/10.1016/j.atmosenv.2008.10.057>, 2009.
- 706 Tadić, J. M., Michalak, A. M., Iraci, L., Ilić, V., Biraud, S. C., Feldman, D. R., Bui, T., Johnson,  
707 M. S., Loewenstein, M., Jeong, S., Fischer, M. L., Yates, E. L., and Ryoo, J.-M.: Elliptic  
708 Cylinder Airborne Sampling and Geostatistical Mass Balance Approach for Quantifying  
709 Local Greenhouse Gas Emissions, *Environ. Sci. Technol.*, 51, 10012–10021,  
710 <https://doi.org/10.1021/acs.est.7b03100>, 2017.
- 711 Tang, W., Edwards, D. P., Emmons, L. K., Worden, H. M., Judd, L. M., Lamsal, L. N., Al-Saadi,  
712 J. A., Janz, S. J., Crawford, J. H., Deeter, M. N., Pfister, G., Buchholz, R. R., Gaubert, B.,  
713 and Nowlan, C. R.: Assessing sub-grid variability within satellite pixels over urban  
714 regions using airborne mapping spectrometer measurements, 14, 4639–4655,  
715 <https://doi.org/10.5194/amt-14-4639-2021>, 2021.
- 716 Valin, L. C., Russell, A. R., Hudman, R. C., and Cohen, R. C.: Effects of model resolution on the  
717 interpretation of satellite NO<sub>2</sub> observations, 11, 11647–11655,  
718 <https://doi.org/10.5194/acp-11-11647-2011>, 2011.
- 719 Vinken, G. C. M., Boersma, K. F., Jacob, D. J., and Meijer, E. W.: Accounting for non-linear  
720 chemistry of ship plumes in the GEOS-Chem global chemistry transport model, 11,  
721 11707–11722, <https://doi.org/10.5194/acp-11-11707-2011>, 2011.
- 722 Wang, P., Peters, A., van Geffen, J., Tuinder, O., Stammes, P., and Kinne, S.: Shipborne MAX-  
723 DOAS measurements for validation of TROPOMI NO<sub>2</sub> products, 13, 1413–1426,  
724 <https://doi.org/10.5194/amt-13-1413-2020>, 2020.



- 725 Wang, Y., Sabatino, S. D., Martilli, A., Li, Y., Wong, M. S., Gutiérrez, E., and Chan, P. W.:  
726 Impact of land surface heterogeneity on urban heat island circulation and sea-land breeze  
727 circulation in Hong Kong, 122, 4332–4352, <https://doi.org/10.1002/2017JD026702>,  
728 2017.
- 729 Wolfe, G. M., Nicely, J. M., Clair, J. M. S., Hanisco, T. F., Liao, J., Oman, L. D., Brune, W. B.,  
730 Miller, D., Thames, A., Abad, G. G., Ryerson, T. B., Thompson, C. R., Peischl, J.,  
731 McKain, K., Sweeney, C., Wennberg, P. O., Kim, M., Crounse, J. D., Hall, S. R.,  
732 Ullmann, K., Diskin, G., Bui, P., Chang, C., and Dean-Day, J.: Mapping hydroxyl  
733 variability throughout the global remote troposphere via synthesis of airborne and  
734 satellite formaldehyde observations, PNAS, 116, 11171–11180,  
735 <https://doi.org/10.1073/pnas.1821661116>, 2019.
- 736 Wu, C.-D., Zeng, Y.-T., and Lung, S.-C. C.: A hybrid kriging/land-use regression model to  
737 assess PM<sub>2.5</sub> spatial-temporal variability, Science of The Total Environment, 645, 1456–  
738 1464, <https://doi.org/10.1016/j.scitotenv.2018.07.073>, 2018.
- 739 Yu, K., Jacob, D. J., Fisher, J. A., Kim, P. S., Marais, E. A., Miller, C. C., Travis, K. R., Zhu, L.,  
740 Yantosca, R. M., Sulprizio, M. P., Cohen, R. C., Dibb, J. E., Fried, A., Mikoviny, T.,  
741 Ryerson, T. B., Wennberg, P. O., and Wisthaler, A.: Sensitivity to grid resolution in the  
742 ability of a chemical transport model to simulate observed oxidant chemistry under high-  
743 isoprene conditions, 16, 4369–4378, <https://doi.org/10.5194/acp-16-4369-2016>, 2016.
- 744 Zhan, Y., Luo, Y., Deng, X., Zhang, K., Zhang, M., Grieneisen, M. L., and Di, B.: Satellite-  
745 Based Estimates of Daily NO<sub>2</sub> Exposure in China Using Hybrid Random Forest and  
746 Spatiotemporal Kriging Model, Environ. Sci. Technol., 52, 4180–4189,  
747 <https://doi.org/10.1021/acs.est.7b05669>, 2018.
- 748 Zhao, X., Griffin, D., Fioletov, V., McLinden, C., Cede, A., Tiefengraber, M., Müller, M.,  
749 Bogner, K., Strong, K., Boersma, F., Eskes, H., Davies, J., Ogyu, A., and Lee, S. C.:  
750 Assessment of the quality of TROPOMI high-spatial-resolution NO<sub>2</sub> data products in the  
751 Greater Toronto Area, 13, 2131–2159, <https://doi.org/10.5194/amt-13-2131-2020>, 2020.  
752

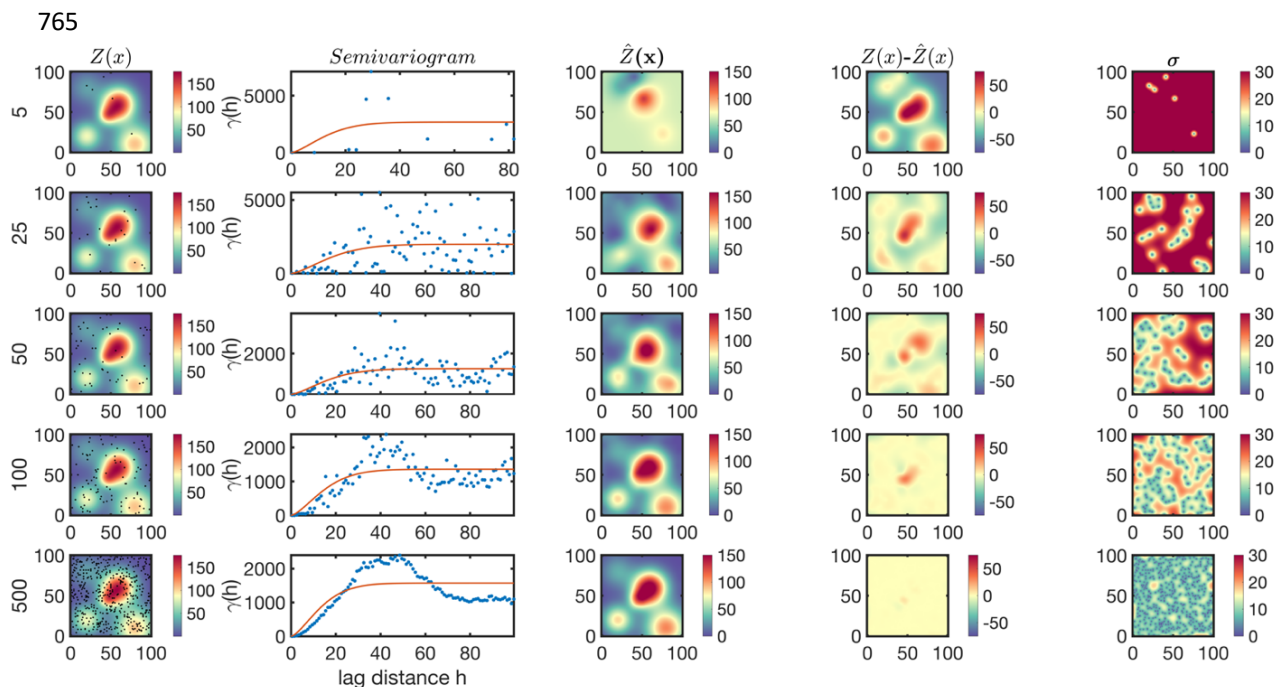


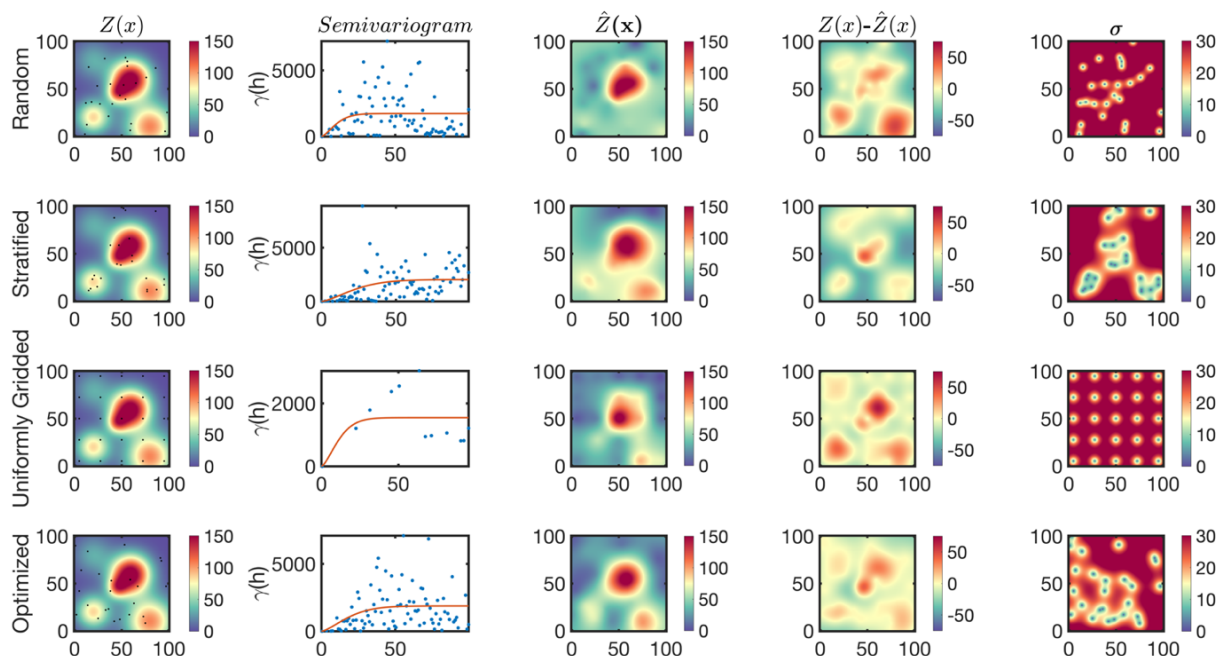
753 Figures:



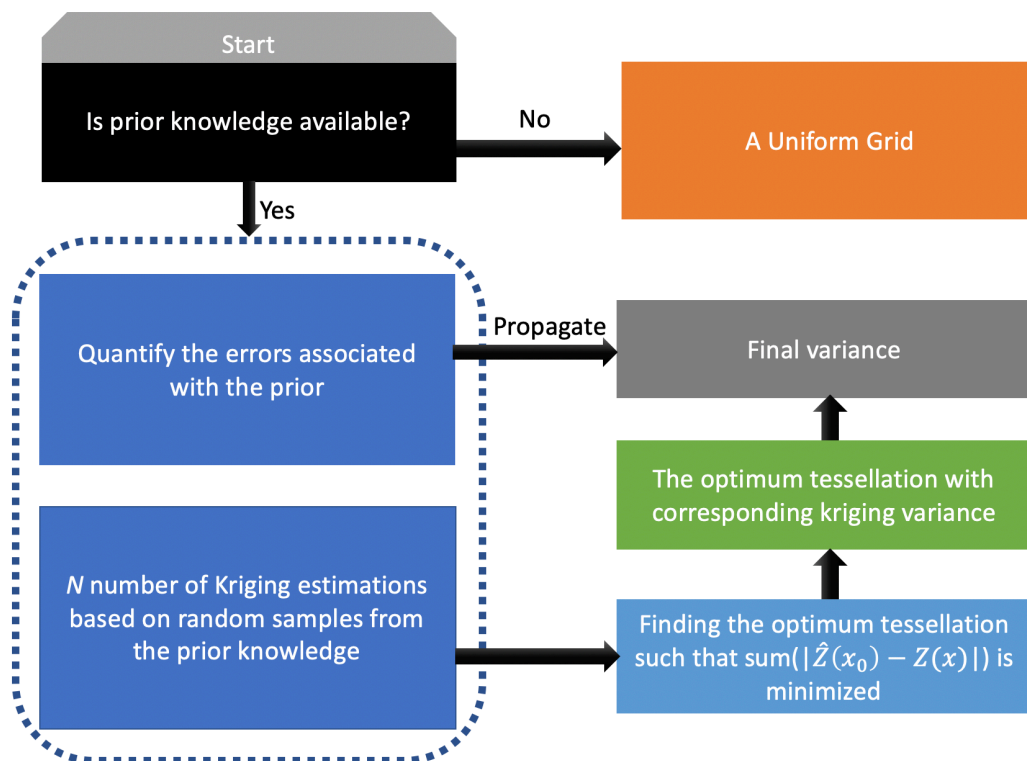
755 **Figure 1.** (first column) Five theoretical fields randomly sampled with 200 points (dots), namely,  
 756 a constant field (C1), a ramp starting from zero in the lower left to higher values in the upper right  
 757 (C2), an intersection with concentrated values in four corridors (C3), a Gaussian plume placed in  
 758 the center (C4), and multiple Gaussian plumes spread over the entire domain (C5). (second column)  
 759 the corresponding isotropic semivariograms computed based on Eq.2; the red line shows the stable  
 760 Gaussian fitted to the semivariogram based on Levenberg-Marquardt method. (third column) The  
 761 kriging estimate at the same resolution of the truth (i.e.,  $1 \times 1$ ) based on Eq.6. (fourth column) The  
 762 difference between the estimate and the truth. (fifth column) the kriging standard error based on  
 763 Eq.11.

764

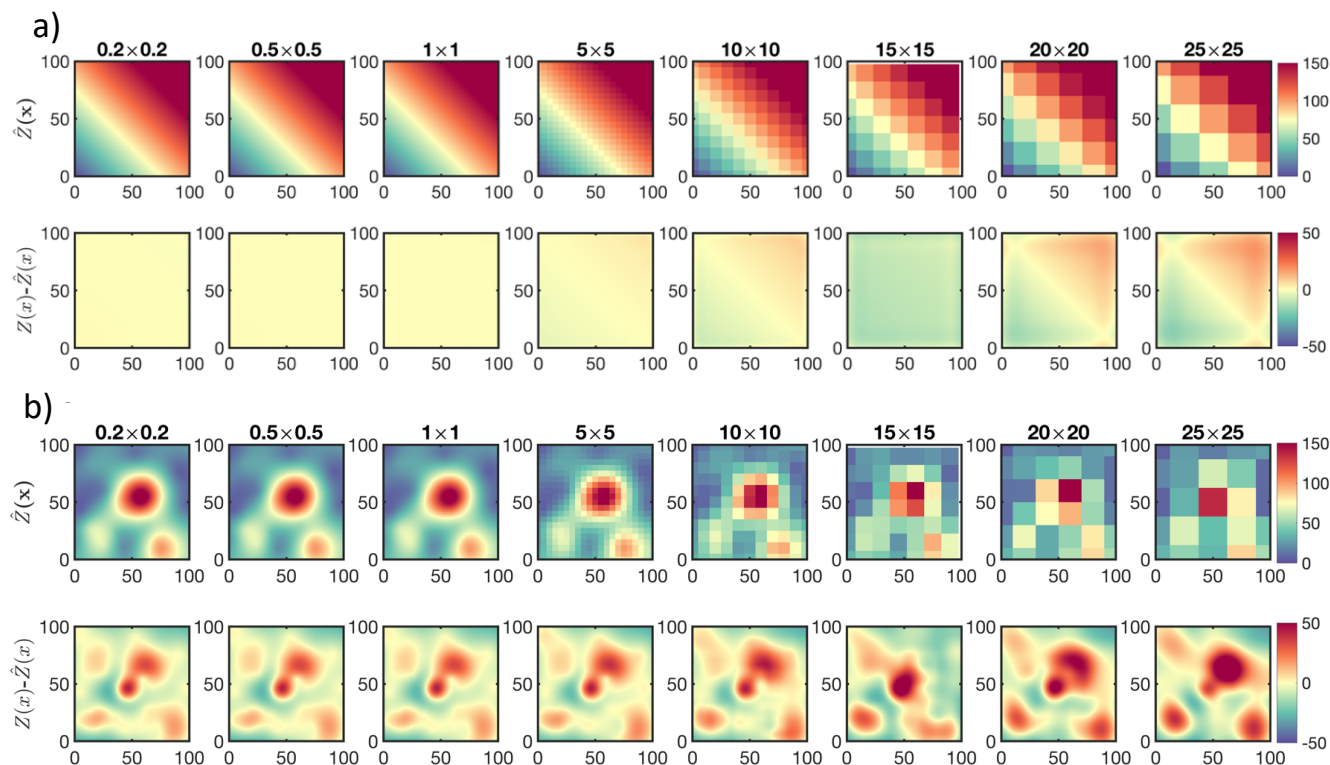




774 **Figure 3.** The multi-plume case (C5) randomly sampled by four different sampling strategies  
775 using a constant number of samples (25). The sampling strategies include purely random (first  
776 row), stratified random (second row), uniform grids (third row), and an optimized tessellation  
777 proposed based on kriging (fourth row). Columns represent the truth, the isotropic semivariogram,  
778 the kriging estimate, the difference between the estimate and the truth, and the kriging standard  
779 error.  
780

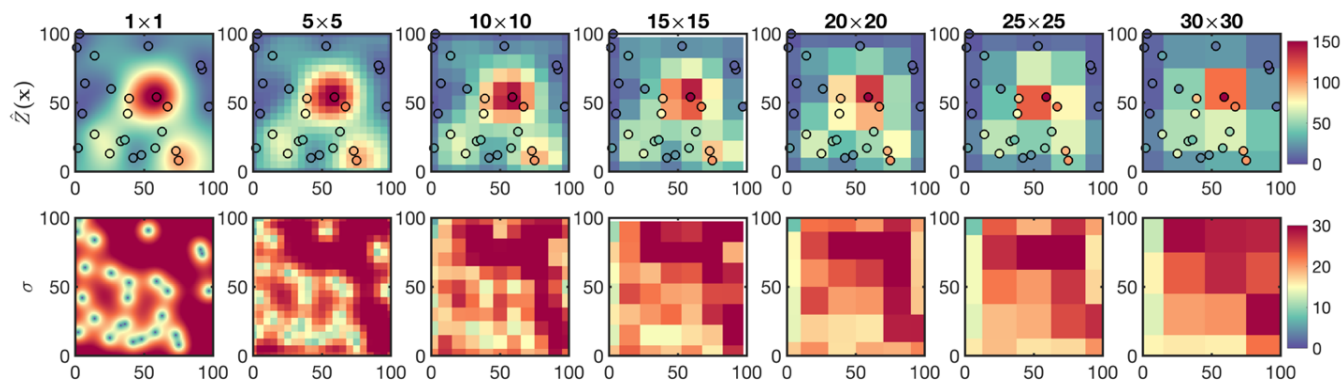


781  
782 **Figure 4.** A schematic illustrating a framework for optimum sampling (tessellation) strategy. The  
783 prior knowledge refers to any data being able of describing our quantity of interest including site-  
784 visits, theoretical models, satellite observations, emissions, and etc.  
785  
786



789 **Figure 5.** Finding an optimum grid cell for kriging. (a) The kriging estimates of the ramp (C2) at  
790 different grid resolutions ranging from  $25 \times 25$  pixel to  $0.2 \times 0.2$ . (b) The kriging estimates of the  
791 multi-plume (C5) with optimized samples shown in Figure 3 for different grid resolutions. C2 is  
792 more homogeneous than C5, as a result, it is less sensitive to the resolution of the kriging  
793 estimate. The optimum grid resolution for C2 is  $10 \times 10$ , whereas it is  $1 \times 1$  for C5. These numbers  
794 are based on observing negligible difference ( $< 1\%$ ) between the kriging estimate at the optimum  
795 resolution and the one computed at a finer resolution step. We call the optimum output for C5 as  
796 C5opt.

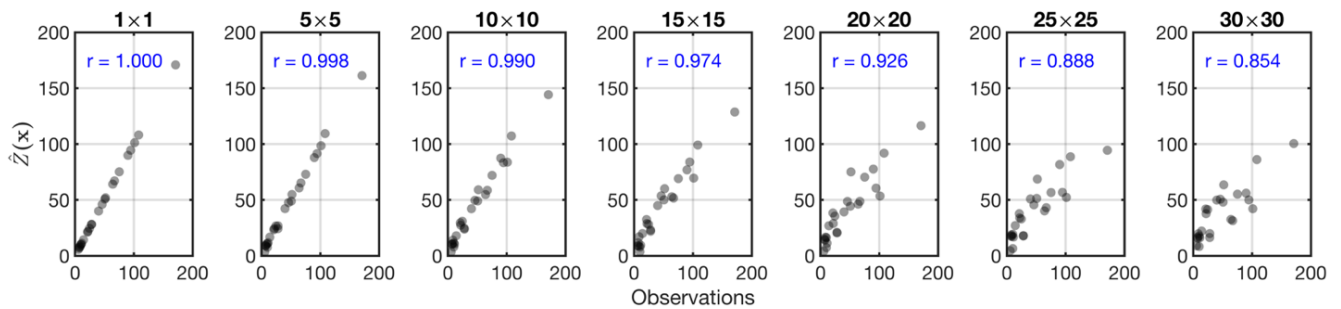
797  
798  
799



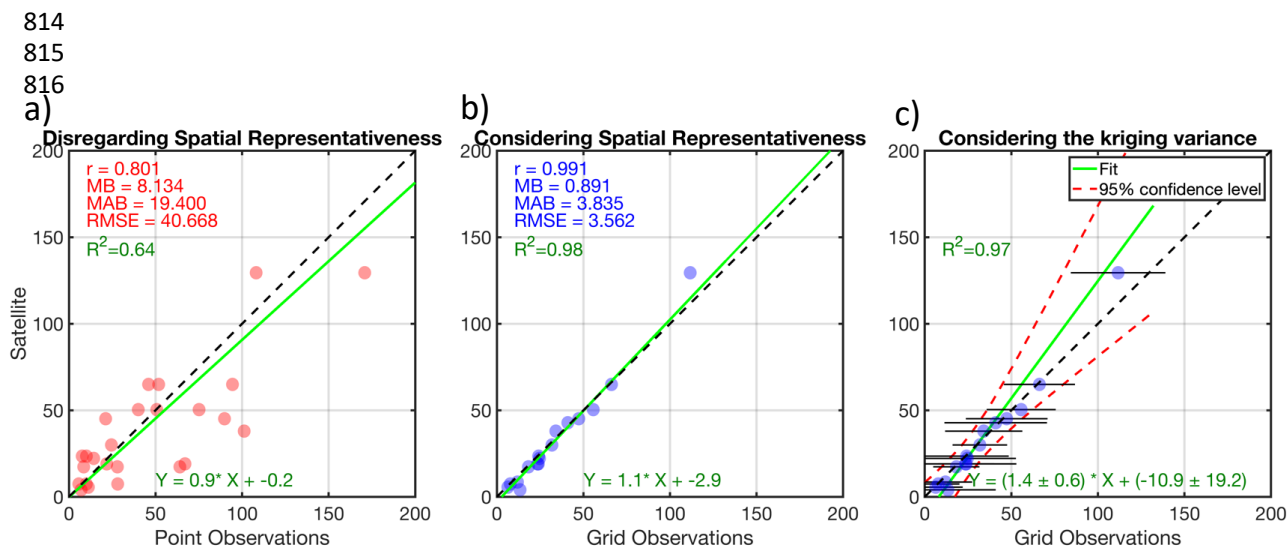
801 **Figure 6.** (first row) C5Opt outputs convolved with an ideal box kernel with different sizes ( $1 \times 1$   
802 up to  $30 \times 30$ ) overlaid by the C5Opt optimum samples. (second row) the associated kriging errors  
803 convolved with the same kernel. The coarser the resolution is, the larger the discrepancy between  
804 the samples and the estimates is.

805  
806  
807  
808

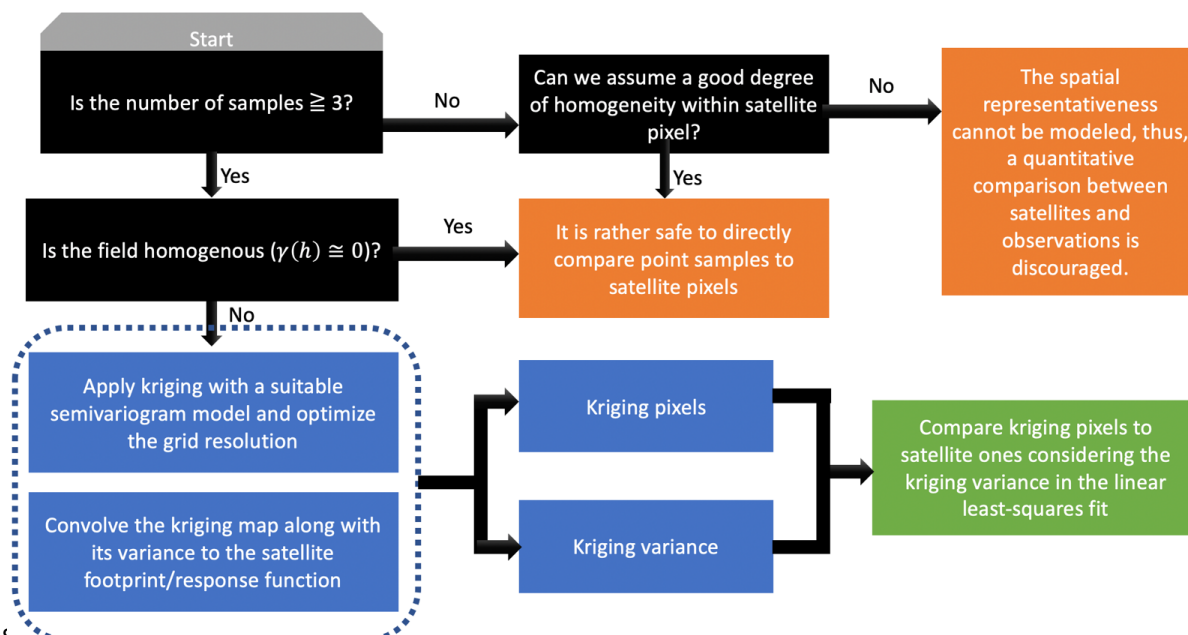




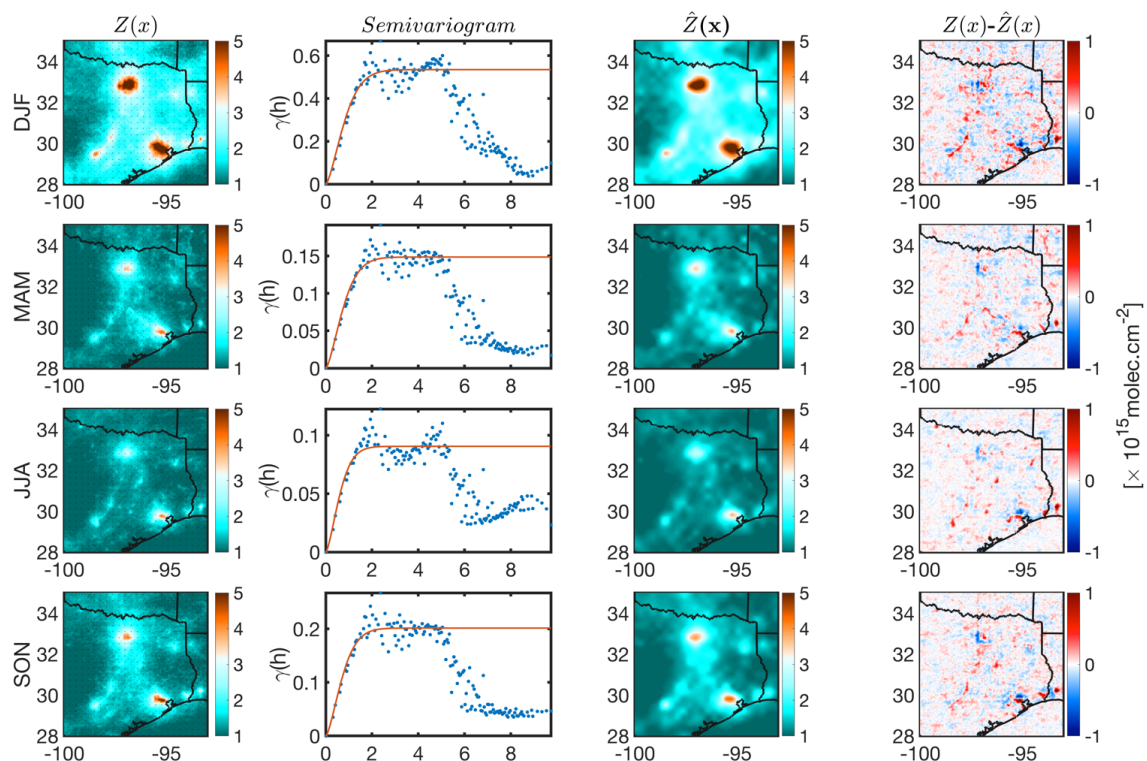
810 **Figure 7.** Illustrating the problem of spatial scale: comparisons of the kriging estimates at seven  
811 different spatial scales with the samples used for the C5opt estimation. The perceived  
812 discrepancies are purely due to the spatial representativeness.  
813



818  
 819 **Figure 8.** (a) the direct comparison of pseudo observations of a satellite observing the C5 case at  
 820  $30 \times 30$  resolution versus the 25 samples used for C5opt. (b) same for y-axis, but the point samples  
 821 are transformed to grids using kriging convolved with the satellite spatial response function (ideal  
 822 box with  $30 \times 30$  kernel size). The differences in statistics between these two experiments speak to  
 823 the problem of scale. (b) ignores the kriging errors but (c) incorporates them using a Monte Carlo  
 824 method. Note that the best linear fit has changed indicating that the consideration of the kriging  
 825 variance is critical. MB = mean bias (point minus satellite), MAB = mean absolute bias, RMSE =  
 826 root mean square error,  $R^2$  = coefficient of determination.  
 827



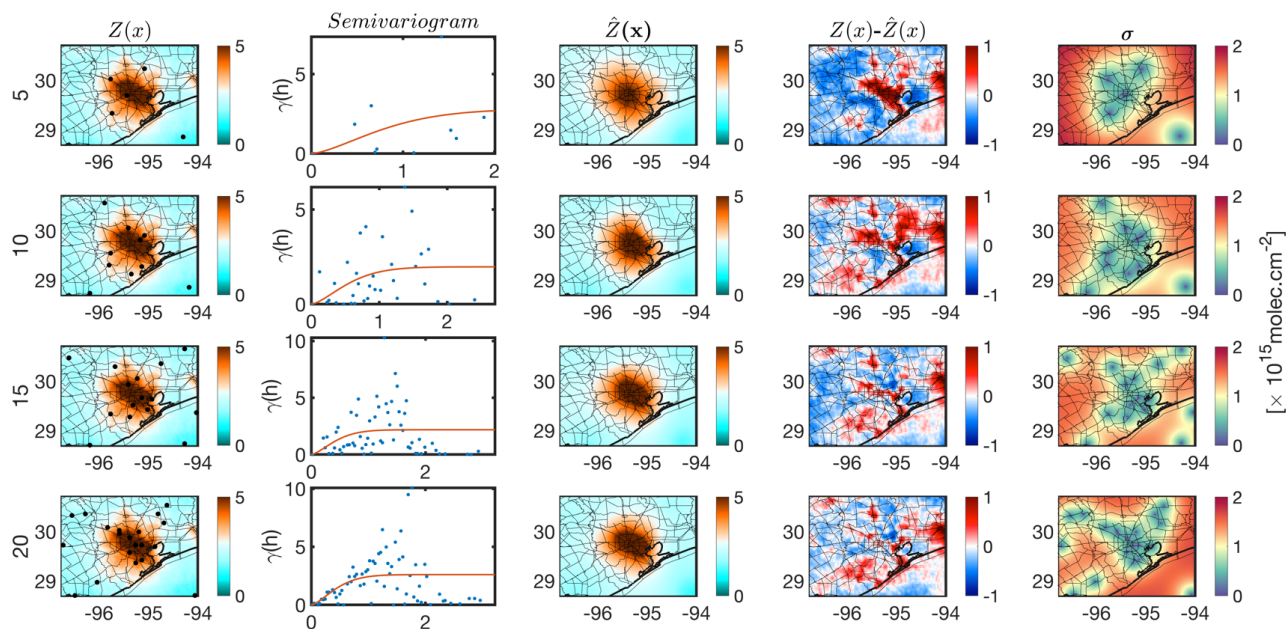
828  
829 **Figure 9.** The proposed roadmap for transforming pointwise measurements to gridded data in  
830 satellite (model) validation.  
831



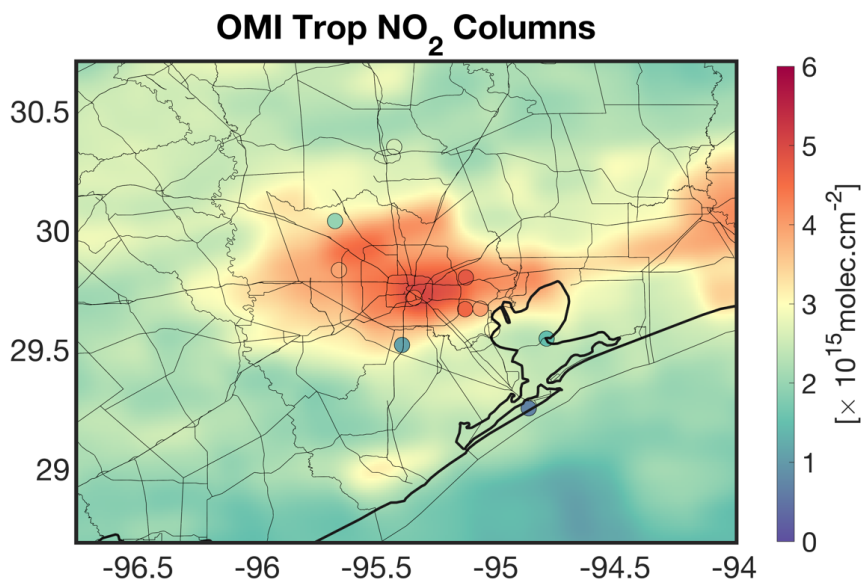
8  
833 **Figure 10.** (first column) The spatial distribution of TROPOMI tropospheric NO<sub>2</sub> columns  
834 oversampled in four different seasons at 3×3 km<sup>2</sup> spatial resolution. (second column) The  
835 corresponding semivariogram from samples selected from uniform 30×30 km<sup>2</sup> blocks (shown  
836 with black dots in the first column) along the fitted stable Gaussian model (red line). (third  
837 column) the kriging estimates, and (fourth column) their differences with respect to the  
838 observations.  
839  
840



841



843 **Figure 11.** Finding an optimum sample tessellation for wintertime over Houston given different  
844 number of spectrometers (5, 10, 15, and 20).  
845

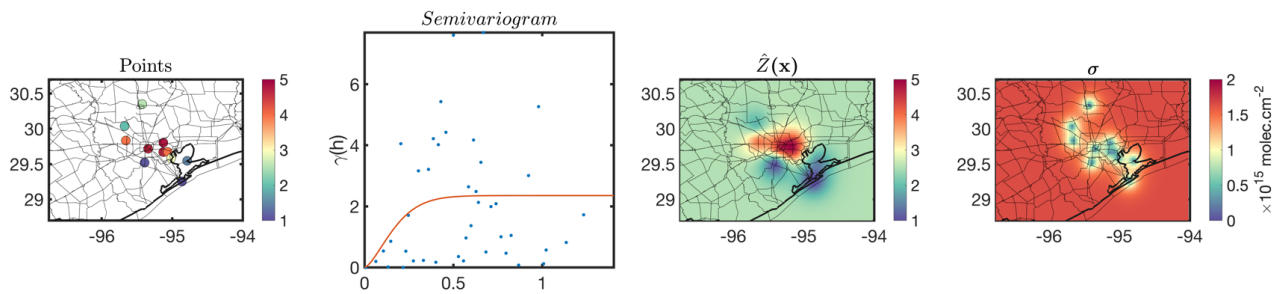


846  
847  
848  
849  
850  
851  
852  
853  
854

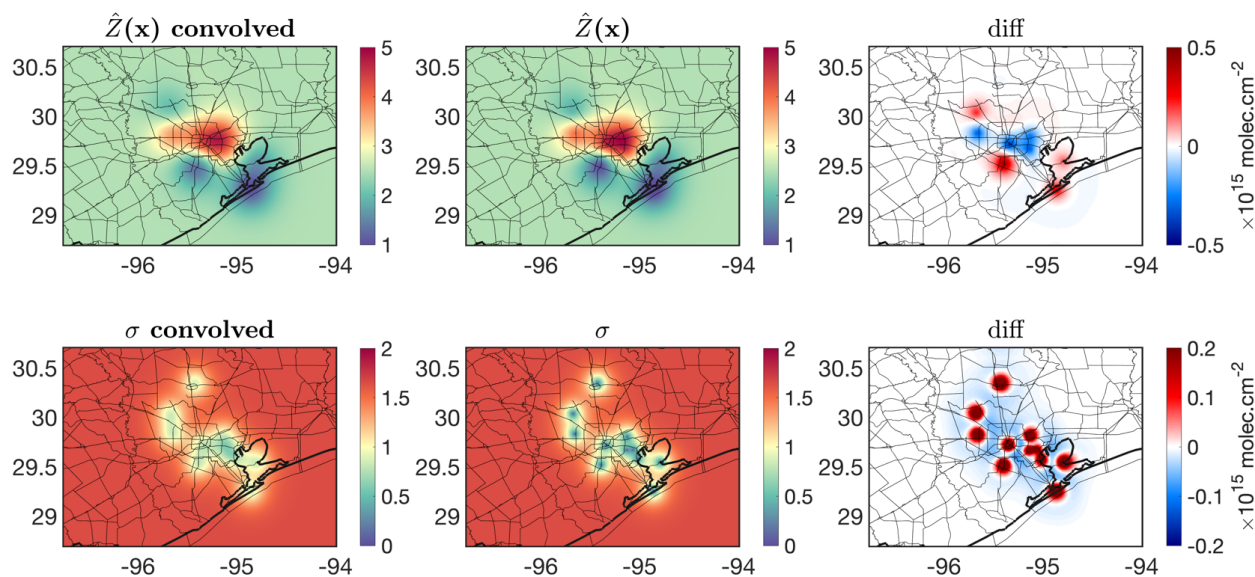
**Figure 12.** The spatial distribution of OMI tropospheric NO<sub>2</sub> columns oversampled at the resolution at 20×20 km<sup>2</sup> over Houston in September 2013. The plot is overlaid by surface Pandora spectrometer instrument averaged over the same month. The surface measurements originally measured the total columns, therefore we subtract their values from the stratospheric columns provided by the OMI data ( $2.8 \pm 0.16 \times 10^{15}$  molecules cm<sup>-2</sup>) to focus on the tropospheric part.



855  
856

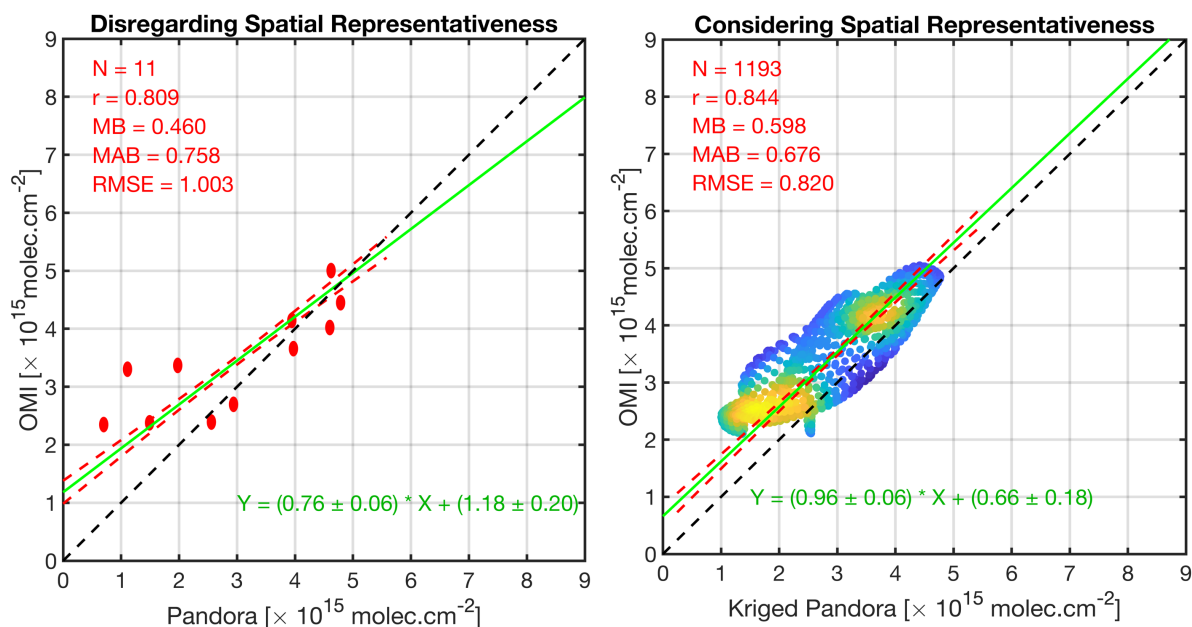


858 **Figure 13.** The Pandora tropospheric NO<sub>2</sub> measurements (made from subtracting the total columns  
859 from the OMI stratospheric NO<sub>2</sub> columns) during September 2013, the corresponding  
860 semivariogram, the kriging estimates, and the kriging standard errors. Note that the semivariogram  
861 suggests a large degree of spatial heterogeneity occurring at different spatial scales.  
862



8  
864 **Figure 14.** Convoluting both kriging estimates and errors with the OMI spatial response function  
865 formulated in Sun et al. [2018]. The differences against the pre-convolved fields are also depicted.  
866





868

869 **Figure 15.** (left): the direct comparison of OMI tropospheric NO<sub>2</sub> columns with 11 pointwise  
870 Pandora measurements in September 2013 over Houston. (right) same for y-axis, but the PSI  
871 measurements are translated to grids using kriging convolved with the OMI spatial response  
872 function. PSI tropospheric NO<sub>2</sub> columns are estimated based on subtracting their total columns  
873 from the OMI stratospheric NO<sub>2</sub> ones ( $2.8 \pm 0.16 \times 10^{15}$  molecules cm<sup>-2</sup>). We only consider kriging  
874 estimates whose errors are below  $1.2 \times 10^{15}$  molecules cm<sup>-2</sup>. The kriging variances are also  
875 considered using the Monte Carlo method on  $\chi^2$ . The slope has improved after considering the  
876 modeled spatial representativeness. MB = mean bias (OMI vs Pandora), MAB = mean absolute  
877 bias, RMSE = root mean square error.

878